

Phase-field model of vapor-liquid-solid nanowire growth

Nan Wang¹, Moneesh Upmanyu², and Alain Karma¹

¹*Physics Department and Center for Interdisciplinary Research on Complex Systems,
Northeastern University, Boston, Massachusetts 02115, USA*

²*Department of Mechanical and Industrial Engineering,
Northeastern University, Boston, Massachusetts 02115, USA**

(Dated: October 27, 2017)

We present a multi-phase-field model to describe quantitatively nanowire growth by the vapor-liquid-solid (VLS) process. The free-energy functional of this model depends on three non-conserved order parameters that distinguish the vapor, liquid, and solid phases and describes the energetic properties of various interfaces, including arbitrary forms of anisotropic γ -plots for the solid-vapor and solid-liquid interfaces. The evolution equations for those order parameters describe basic kinetic processes including the rapid (quasi-instantaneous) equilibration of the liquid catalyst to a droplet shape with constant mean curvature, the slow incorporation of growth atoms at the droplet surface, and crystallization within the droplet. The standard constraint that the sum of the phase fields equals unity and the conservation of the number of catalyst atoms, which relates the catalyst volume to the concentration of growth atoms inside the droplet, are handled via separate Lagrange multipliers. An analysis of the model is presented that rigorously maps the phase-field equations to a desired set of sharp-interface equations for the evolution of the phase boundaries under the constraint of force-balance at three-phase junctions (triple points) given by the Young-Herring relation that includes torque term related to the anisotropy of the solid-liquid and solid-vapor interface excess free energies. Numerical examples of growth in two dimensions are presented for the simplest case of vanishing crystalline anisotropy and the more realistic case of a solid-liquid γ -plot with cusped minima corresponding to two sets of (10) and (11) facets. The simulations reproduce many of the salient features of nanowire growth observed experimentally, including growth normal to the substrate with tapering of the side walls, transitions between different growth orientations, and crawling growth along the substrate. They also reproduce different observed relationships between the nanowire growth velocity and radius depending on the growth condition. For the basic normal growth mode, the steady-state solid-liquid interface tip shape consists of a main facet intersected by two truncated side facets ending at triple points. The ratio of truncated and main facet lengths are in quantitative agreement with the prediction of sharp-interface theory that is developed here for faceted nanowire growth in two dimensions.

I. INTRODUCTION

Semiconductor nanowires (NWs) have emerged as promising small building blocks for various nanotechnology applications ranging from nanoelectronics to sensors to solar energy harvesting. The functional properties of these NWs can be tuned by controlling their chemical composition and growth morphologies, and hence a fundamental understanding of the underlying crystal growth has been the subject of much recent research [1–3]. A well-studied NW synthesis route is vapor-liquid-solid (VLS) growth. In this process, small liquid droplets of a metallic element (e.g. Au) are deposited on an initially flat solid substrate of the NW element (e.g. Si). The droplet surfaces act as preferential sites for the capture of growth atoms by catalytic breakdown of a molecular gas (e.g. Si₂H₆). The bulk of the alloy droplet in turn acts as a conduit of these atoms to the solid, thereby facilitating the growth of solid regions capped by liquid droplets, which emerge as NWs from the substrate.

VLS growth has been widely studied experimentally and theoretically during the past decade. Experiments

have revealed a wealth of interesting growth behaviors [4–6]. While NWs commonly grow normal to the substrate along some preferred crystallographic directions (e.g. $\langle 111 \rangle$ for Si), they can also grow at an angle to the substrate [7, 8], change growth directions after emerging from the substrate following kinked or more erratic trajectories, or crawl along the substrate [9]. Furthermore, NWs exhibit intricate solid-liquid and solid-vapor interface morphologies [10]. The solid-liquid interface typically consists of a main facet normal to the NW growth direction, but also small side facets ending at a triple line where vapor, liquid, and solid phases meet. The solid-vapor interface that shapes the NW sidewalls consists of different sets of facets that can be smooth or sawtooth-like [11]. There has been theoretical progress to address various aspects of NW growth using analytical [12–18], numerical continuum models [19–27] and molecular dynamics simulations [28–30]. Some of those studies have shed light on the relationship of the NW growth rate and radius under steady-state growth conditions [13–15], the selection of the radius for prescribed liquid catalyst volume [16], the stability and shape changes of liquid droplets, the oscillatory behavior of side solid-liquid facets and the growth orientation selection [17, 18, 26].

Despite this progress, modeling NW growth quantita-

* Corresponding author: Alain Karma, email: a.karma@neu.edu

tively on continuum scales remains a major challenge. A main difficulty is the fact that both solid-liquid and solid-vapor interfaces are faceted and undergo complex shape changes during NW formation. For example, as the NW first emerges from the substrate, the equilibrium solid-liquid interface shape changes from concave to convex and the solid-vapor interface changes orientation as the NW develops a tapered shape. Tracking the evolution of faceted solid-liquid and solid-vapor interfaces under the constraint that different facets meet with the isotropic liquid-vapor interface at the triple line is a daunting task. To this end, Schwarz and Tersoff (ST) developed a continuum model that tracks the evolution of anisotropic non-faceted interfaces, demonstrating the ability of this model to simulate the complete evolution of a deposited droplet into a NW [19–23]. They further extended this model to faceted interfaces, reproducing qualitatively non-trivial growth behaviors such as NW kinking and crawling. Despite its success to reproduce a number of observed growth modes, this approach relies on phenomenological parameters and rules to model the energetics and dynamics of facet creation. In addition, it tracks interfaces explicitly as sharp boundaries, which makes its extension to 3D difficult.

Phase-field modeling provides an attractive alternative to interface tracking methods to model VLS growth at the continuum scale. This method is well-known for its ability to circumvent the difficulty of interface tracking by making interfaces spatially diffuse [31–34, 36–39]. Furthermore, by use of more than one scalar order parameters, it can naturally distinguish several phases, thereby handling complex geometries and changes of interface topology. However, the application of the phase-field method to VLS growth remains limited to date. One set of studies used a phase-field model with viscous flow to investigate some dynamical aspects of liquid droplet wetting and shape stability [25]. Another study introduced a multiphase-field model that uses a non-standard hybrid of Ginzburg-Landau and Cahn-Hilliard dynamics to conserve the volume of the liquid catalyst [27]. This model was used to produce 3D NW growth morphologies that resemble observed morphologies. However, the sharp-interface limit of this model was not analyzed in detail and simulations were carried out for analytical forms of crystalline anisotropy corresponding to non-faceted interfaces.

In this paper, we develop a phase-field model to simulate quantitatively NW growth for realistic forms of crystalline anisotropy corresponding to faceted interfaces. We carry out a detailed asymptotic analysis of the model in the limit where the interface thickness is small compared to the NW radius. This analysis maps the phase-field dynamical equations onto a well-defined set of sharp-interface equations, thereby allowing us to relate phase-field model and materials parameters. Furthermore, we present 2D simulations that illustrate how the model can reproduce salient features of NW growth including tapered growth normal to the substrate, kinking, and

crawling. At a more quantitative level, we validate the model by comparison of 2D phase-field simulations to predictions of sharp-interface theory. This comparison is made for the NW growth rate and radius as well as for the faceted shape of the solid-liquid interface during steady-state growth at constant velocity.

A. Phase-field formulation

We develop a multiphase-field formulation with three scalar order parameters that distinguish the solid, liquid and vapor phases, and with a free-energy form adapted from a previous model of eutectic growth [40]. We derive relations that relate this free-energy functional to energetic properties of various interfaces, including arbitrary forms of anisotropic γ -plots for the solid-vapor and solid-liquid interfaces. The evolution equations for those order parameters describe basic kinetic processes including the rapid (quasi-instantaneous) equilibration of the liquid catalyst to a droplet shape with constant mean curvature, the catalytic incorporation of growth atoms at the droplet surface, and crystallization within the droplet. The standard constraint that the sum of the phase fields equals unity and the conservation of the number of catalyst atoms, which relates the catalyst volume to the concentration of growth atoms inside the droplet, are handled via separate Lagrange multipliers.

Two physically distinct growth situations are modeled. The first is the one considered by ST where the NW growth rate is limited by the incorporation rate of growth atoms at the droplet surface. In this situation, the change of the droplet volume is governed by the balance of the fluxes of growth atoms into and out of the droplet, assumed to contain a fixed number of catalyst atoms. During steady-state growth those two fluxes must balance each other. The rate of incorporation of growth atoms into the droplet is the product of the droplet surface area and a constant surface flux J , defined as the number of growth atoms incorporated per unit time per unit area of droplet surface, while the incorporation rate into the solid scales as the product of the NW growth rate V and solid-liquid interface area divided by the atomic volume of solid Ω_s . Since both the droplet surface area and solid-liquid interface area scale as R^{d-1} (where d is the spatial dimension), $V \sim J\Omega_s$ is independent of NW radius in this limit, as observed in some experiments [5]. The second limit we consider is the one where growth is limited by the solid-liquid interface kinetics and the chemical potential of growth atoms can be assumed to be equal in the liquid and vapor and constant in time, i.e. those two phases equilibrate quickly on the time scale where the solid adds one additional layer of atoms. In this case, the chemical driving force for growth (difference of chemical potential between liquid and solid) is reduced by interface curvature and the growth rate depends on NW radius as predicted by some sharp-interface theories and observed in other experiments [13, 14].

B. Faceted interfaces

A general difficulty in modeling faceted interfaces is that the γ -plot exhibit cusps at faceted orientations. A cusp is reflected in the anisotropy of the interface free-energy, which can be written near a facet in the form

$$\gamma(\theta) = \gamma_f(1 + \delta_f|\theta - \theta_f| + \dots) \quad (1)$$

where θ denotes the angle of the normal to the interface with respect to a fixed reference crystal axis, γ_f is the facet free-energy at angle $\theta = \theta_f$, and the above form is valid for a vicinal interface where $|\theta - \theta_f| \ll 1$. Such an interface is generally composed of steps spaced a distance $d \approx h/|\theta - \theta_f|$ where h is the step height. The excess interface free-energy associated with step formation is therefore γ_s/d , where γ_s is the isolated step free-energy (with unit of energy per unit length of step). It follows that the total excess free-energy of the vicinal interface is given by Eq. 1 with $\delta_f = \gamma_s/(\gamma_f h)$. Cusps make the function $\gamma(\theta)$ non-differentiable. This poses a difficulty in phase-field modeling where the evolution equation for a given phase-field ϕ distinguishing two phases is derived from a first variation of a free-energy functional that contains the function $\gamma(\hat{n})$ with the interface normal expressed as $\hat{n} = -\vec{\nabla}\phi/|\nabla\phi|$. To overcome this difficulty, we follow the method previously developed for faceted dendritic solidification that consists of rounding the cusp over a small range of angle so as to make $\gamma(\theta)$ differentiable [41].

In this paper, cusp-rounding is implemented by using the function $\sqrt{\epsilon^2 + x^2}$ that converges to the absolute value function $|x|$ in the limit $\epsilon \rightarrow 0$. This approach is conceptually similar to the approach followed in Ref. [41], but easier to implement computationally. Importantly, results do not depend sensitively on cusp-rounding for small values $\epsilon \sim 10^{-2}$. Furthermore, we consider a simple form of solid-liquid γ -plot with two sets of (10) and (11) facets. For a crystal seed surrounded by liquid, this γ -plot yields an octagonal faceted equilibrium crystal shape with four facets of each type. This shape is easily predicted by the standard Wulff construction. For NW growth from a (10) substrate, this γ -plot yields a solid-liquid interface shape consisting of a main (10) facet intersected by two truncated (11) and (11) side facets ending at triple points, which is qualitatively similar to the interface shape observed experimentally and in MD simulations. In this more complex geometry, the Wulff construction is not sufficient to predict the interface shape because side facets end at triple points. To predict this shape, we follow two equivalent approaches within a sharp-interface picture.

The first approach is to apply the Wulff construction, expressed in a parametric representation where the cartesian coordinates of the interface are functions of θ , together with the anisotropic Young-Herring's condition of thermomechanical equilibrium at triple points[42]. This

conditions is given by

$$\gamma_{lv}\hat{t}_{lv} + \gamma_{sl}\hat{t}_{sl} + \gamma_{sv}\hat{t}_{sv} + \gamma'_{sl}\hat{n}_{sl} = 0, \quad (2)$$

where γ_{lv} , γ_{sl} , and γ_{sv} are the liquid-vapor, solid-liquid, and solid-vapor interfacial energies, respectively, $\hat{t}_{\alpha\beta}$ and $\hat{n}_{\alpha\beta}$ are the unit vectors tangent and perpendicular to the $\alpha\beta$ interface, respectively, and $\gamma'_{sl} \equiv \partial\gamma_{sl}/\partial\theta$. This ‘‘torque’’ term tends to rotate the solid-liquid interface towards a low-energy faceted orientation. A similar term also applies to the anisotropic solid-vapor interface but is omitted here since it does not influence steady-state NW growth with vertical side walls. Note that the torque term is uniquely determined when the cusp is rounded and $\gamma_{sl}(\theta)$ is differentiable. In this case, the parametric equation for the interface shape together with Eq. 2 uniquely determines this shape. Importantly, this shape converges to a unique, physically desired, faceted shape in the $\epsilon \rightarrow 0$ limit.

The second method to obtain the same shape, which serves as an independent check, is to treat directly the case $\epsilon = 0$ without cusp-rounding where γ'_{sl} is not defined at $\theta = \theta_f$ because of the absolute value in Eq. 1. In this case, the shape is found by considering virtual displacements of facets and triple points that leave the total free-energy unchanged. Interestingly, the condition obtained by considering the virtual displacement of a triple point can also be obtained by projecting the Young-Herring condition (2) onto two cartesian axes parallel and perpendicular to the NW growth direction, which yields two equations. The solutions of those two equations for fixed faceted orientations in turn yield the value undetermined of γ'_{sl} at $\theta = \theta_f$, which must physically be comprised in the interval $-\gamma_f\delta_f < \gamma'_{sl} < \gamma_f\delta_f$ following Eq. 1, and a second equation identical to the one obtained by considering a virtual displacement of the triple point that extends the truncated side facet of the solid-liquid interface. This latter condition determines the dihedral angle between the liquid-vapor and solid-liquid interfaces at the triple point. For this reason, in the $\epsilon \rightarrow 0$ limit, the rounded cusp treatment yields the same shape as the one obtained by considering virtual displacements of facets and triple points. We find that this faceted shape predicted by sharp-interface theory is in good quantitative agreement with the one obtained by phase-field simulations. Therefore, in addition to validating our phase-field approach, our results also clarify how sharp-interface theory should be formulated to predict faceted interface shapes during NW growth.

C. Outline

This paper is organized as follows. In the next section, we write down the set of sharp-interface equations used to describe NW growth, which follow closely the model introduced by Schwarz and Tersoff [19]. In section III, we present our multiphase-field model, which is formulated to reduce to the sharp-interface equations of

section II. Various ingredients of the model including the free-energy landscape, the description of the driving force for NW growth, the treatment of Lagrange multipliers to satisfy constraints imposed on the droplet volume and the sum of phase fields, the evolution of the concentration within the droplet, interface mobility, and interface free-energy, are summarized in separate subsections. The equations of the model are then summarized followed by a description of the treatment of anisotropic interfaces in the last subsection. Next, in section IV, we analyze the sharp-interface limit of the model. This analysis is used to pinpoint the conditions under which this limit reduces to the desired set of sharp-interface equations and to relate phase-field parameters to materials parameters. Various numerical examples are then presented in section V. The dependence of the NW growth velocity on radius is characterized in different limits for isotropic interface energies and simulations of faceted growth are compared to the predictions of sharp-interface theory. Conclusions are presented in the last section.

II. SHARP-INTERFACE MODEL

VLS NW growth involves 3 steps essentially [13]: (1) incorporation of Si precursors from the vapor at the vapor-catalyst interface, (2) diffusion of Si atoms through Au catalyst droplet and (3) crystallization at the solid-liquid interface. The ST sharp-interface (SI) model [19] ignores the diffusion process in step (2) and uses a uniform chemical potential within the catalyst droplet since diffusion through the nanoscale liquid droplet is fast compared to the NW growth rate.

The crystallization in step (3) is driven by over-saturation of Si atoms in the catalyst. The NW growth rate v_n is related to the difference of chemical potential between the solid Si and liquid catalyst as

$$v_n = \frac{M_{sl}}{\Omega_s}(\mu_l - \mu_s), \quad (3)$$

assuming a linear dependence. Here, M_{sl} is the solid-liquid interface mobility, Ω_s is the atomic volume of Si atoms in the solid. The liquid concentration is given by $c_l = N_g/(N_c + N_g)$ where N_g is the number of Si growth atoms and N_c the number of catalyst atoms. The chemical potential in the liquid is assumed to be directly related to the over-saturation $c_l - c_0$ as

$$\mu_l = \beta(c_l - c_0) + \Omega_l \gamma_{lv} \kappa_{lv}, \quad (4)$$

where c_0 is the equilibrium concentration and the second term on the right-hand-side is the Gibbs-Thomson correction related to the curvature κ_{lv} of the liquid-vapor surface with energy γ_{lv} . Ω_l is the atomic volume of Si atoms in the liquid and $\beta \equiv \partial\mu_l/\partial c$. The chemical potential in the solid can be written as

$$\mu_s = \Omega_s \left[\left(\gamma_{sl} + \frac{d^2 \gamma_{sl}}{d\theta^2} \right) \kappa_{sl} + p \right]. \quad (5)$$

The first term is the generalized Gibbs-Thomson effect for an anisotropic solid-liquid interfacial free-energy $\gamma_{sl}(\theta)$ where θ is the local surface orientation angle and κ_{sl} is the solid-liquid interface curvature. The second term is a normal force on the solid coming from the liquid internal pressure $p = \gamma_{lv} \kappa_{lv}$. In addition, thermo-mechanical equilibrium at the triple junction of the three (solid, liquid, and vapor) phases imposes a geometrical constraint on the dihedral angles between the phase boundaries at this junction, which is given by the anisotropic Young-Herring's condition (Eq. 2).

To calculate the liquid concentration, the number of Si atoms N_g in the catalyst is tracked during the growth. Assuming a constant flux J on the catalyst surface (the number of Si atoms incorporated at the liquid-vapor surface per unit area per unit time), we have

$$dN_g/dt = \int_{lv} J ds - \Omega_s^{-1} \int_{sl} v_n ds, \quad (6)$$

where ds is the surface element, and v_n is the NW growth velocity. The first integral covers the liquid-vapor surface and accounts for the Si source flux in step (1), the second integral covers the solid-liquid surface and serves as a Si atoms sink due to the crystallization in step (3). During steady-state growth, dN_g/dt in Eq. 6 vanishes and the two fluxes balance each other.

III. PHASE-FIELD MODEL

A. Multiphase-field formulation

To model the VLS NW growth within the PF framework, we build our model on the well established multiphase-field approach developed in the context of multiphase solidification [40]. We use three order parameters ϕ_1 , ϕ_2 and ϕ_3 to distinguish the solid, vapor, and liquid phases, respectively. ϕ_i is the fraction of the i^{th} phase at a given point in space (as depicted in Fig. 1(a)) with constraints $\phi_i \in [0, 1] \forall i$ and

$$\sum_{i=1}^3 \phi_i = 1. \quad (7)$$

The Lyapounov functional representing the total free-energy of this multiphase system is chosen to have a similar form as the Folch-Plapp model of eutectic solidification [40]

$$F = \int \left(\frac{\sigma}{2} f_k + h f_p \right) dv, \quad (8)$$

where σ and h are dimensional constants and dv is the volume element. The first term

$$f_k = \sum_{i=1}^3 |\nabla \phi_i|^2 \quad (9)$$

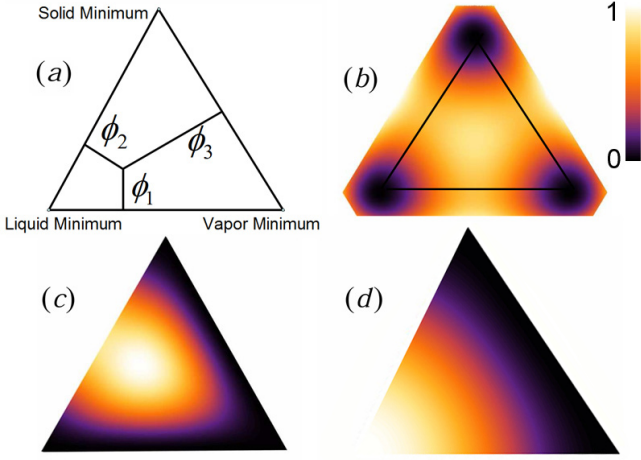


FIG. 1. Basic features of the multiphase-field model used in our formulation. (a) Multiphase-field parameters in a Gibbs triangle. Three bulk phases occupy the 3 vertices of the triangle. The 3 edges correspond to the 3 binary interfaces in the model. A point in the triangle is given by (ϕ_1, ϕ_2, ϕ_3) where ϕ_i is the distance from the given point to the $j-k$ binary interface. (b) Free-energy landscape of the potential term f_p in Eq. 10 with $a_i = b_i = 0$. To highlight the three free-energy minima, the plot range of (ϕ_1, ϕ_2, ϕ_3) is extended beyond $[0,1]$ and thus outside the Gibbs triangle in (a) reproduced as a thick black line. (c) Free-energy landscape of the $a_i f_a^i + b_i f_b$ part in Eq. 10. By setting a non-zero a_2 , it forms an additional barrier along the solid-liquid binary interface and leaves the other two binary interfaces unchanged. b_i controls the height of the triple point ($\phi_1 = \phi_2 = \phi_3 = 1/3$). (d) The function g_l given in Eq. 12. It equals to 1 in the liquid and smoothly decreases to 0 at the solid-vapor binary interface.

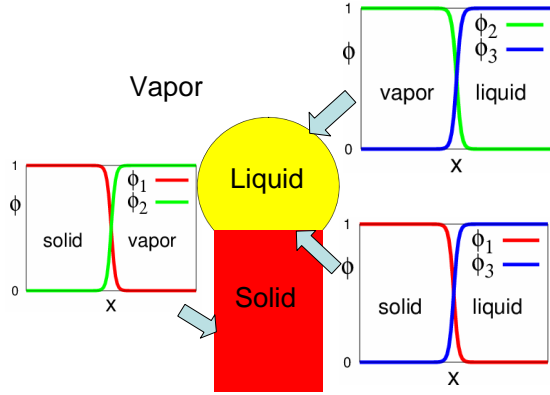


FIG. 2. Outline of the 3 binary interfaces involved in VLS NW growth. The phase fields vary smoothly from 0 to 1 across a spatially diffused interface region with $\phi_1 = 1$, $\phi_2 = 1$, and $\phi_3 = 1$ in solid, vapor, and liquid, respectively.

describes the free-energy cost associated with the spatial variation of the phase-field within the interface regions.

The second term

$$f_p = \sum_{i=1}^3 [f_d^i + a_i f_a^i + b_i f_b], \quad (10)$$

corresponds to the bulk free-energy density with $f_d^i = \phi_i^2(1 - \phi_i)^2$, $f_a^i = \phi_j^2 \phi_k^2 (2\phi_j \phi_k + 3\phi_i)$ and $f_b = \phi_i^2 \phi_j^2 \phi_k^2$. This form yields 3 free-energy minima for the bulk phases with tunable inter-phase barrier heights (Fig. 1(b)). By choosing different a_i , the height of the free-energy barrier between phase j and k can be modified, while leaving the $i-j$ and $i-k$ barriers unaffected. Since this free-energy barrier is linked to the interface energy in the PF model, one can tune the free-energy of any binary interface using this function as shown in later sections. b_i in the last term is multiplied by the square of all three phases. It can be used to vary the height of the three phase junction (triple-point) region in the free-energy landscape (Fig. 1(c)), with the constraint $b_i > 9a_i/2$ ensuring that the triple point is not energetically favored over a binary interface [40]. Increasing b_i decreases the size of the triple-point region. Different choices of this parameter only affect the model behavior within this region but does not change the sharp-interface limit of the model discussed in section IV.

The advantage of the phase-field model is that it satisfies automatically the anisotropic Young-Herring condition that does not need to be imposed as an additional constraint. However, to track the NW growth, a few other conditions also need to be taken into account. In addition to the constraint on the phase fields $\sum_{i=1}^3 \phi_i = 1$, the catalyst volume change needs to be considered during the NW growth. To incorporate that, a modified functional with a Lagrange multiplier λ_A is introduced

$$\tilde{F} = F - \lambda_A h \left[\int g_l(\vec{\phi}) dv - A(t) \right]. \quad (11)$$

$g_l(\vec{\phi})$ is a function that varies smoothly from 1 in the liquid to 0 in the other two phases (Fig. 1(d)) such that its integral over space can be used as a measure of the catalyst size. This additional term ensures that, at given time t , the catalyst area in 2D (volume in 3D) is given by $A(t)$. Specifically, the liquid tilt function g_l is chosen to be

$$g_l = \frac{\phi_3^2}{4} \{ 15(1 - \phi_3)[1 + \phi_3 - (\phi_2 - \phi_1)^2] + \phi_3(9\phi_3^2 - 5) \}. \quad (12)$$

From the modified energy functional \tilde{F} , evolution equations for ϕ_i are derived in a variational form

$$\tau \frac{\partial \phi_i}{\partial t} = - \frac{K(\vec{\phi})}{h} \frac{\delta \tilde{F}}{\delta \phi_i}, \quad (13)$$

where τ is a relaxation time constant and $K(\vec{\phi})$ is a function that can be directly related to the sharp-interface mobility (section IV).

B. Driving force for crystallization

The variational formulation above is just a commonly used scheme to derive PF evolution equations that drive a multiphase system towards a global free-energy minimum. For VLS growth, however, the growth is externally driven by a flux of precursor atoms incorporated at the liquid-vapor interface. This flux maintains a finite supersaturation in the droplet. This supersaturation in turn drives the crystallization of growth atoms at the solid-liquid interface. To account for the fact that this driving force is localized at the solid-liquid interface, we add to the right-hand-side of Eq. 13 a term $\Delta\mu\Omega_s^{-1}u(\phi_1, \phi_3)$ for the evolution of ϕ_1 and ϕ_3 only. Physically, this additional term can be interpreted as the difference of chemical potential of Si atoms between the NW solid and liquid catalyst denoted here by $\Delta\mu$ where the additional factor of Ω_s^{-1} converts the unit of energy per atom of the chemical potential to energy per volume in the PF model. We will derive later an expression for $\Delta\mu$ from the requirement that the evolution of the growth atom concentration in the droplet is the same in the phase-field and sharp-interface models. To localize the driving force for NW growth at the solid-liquid interface, $\Delta\mu$ is multiplied by the function $u(\phi_1, \phi_3) = 15\phi_1^2\phi_3^2$. On the binary solid-liquid interface, where $\phi_3 = 1 - \phi_1$ and $\phi_2 = 0$, this term can be derived variationally from the bulk free-energy density term $-\int d\phi_1 u(\phi_1, 1 - \phi_1)$, which is the standard quintic polynomial used in phase-field models of monophasic solidification that lowers the free-energy of the solid ($\phi_1 = 1$) with respect to the liquid ($\phi_1 = 0$) [48]. The same quintic polynomial is used here to provide the driving force for NW growth. However, because the driving force must be physically localized at the solid-liquid interface, i.e. there is no driving force for the solid to grow into the vapor phase, the $\Delta\mu\Omega_s^{-1}u(\phi_1, \phi_3)$ term is only added to the evolution equation of ϕ_1 and ϕ_3 but not ϕ_2 . This procedure makes the phase-field model globally non-variational since multiphase-field equations with a driving force localized on a specific binary interface cannot be derived in the standard variational form of Eq. 13 by simply adding a free-energy contribution to F that depends on ϕ_1 , ϕ_2 , and ϕ_3 . However, previous studies have shown that non-variational and variational phase-field formulations are equally well-suited to model dendritic solidification as long as they reduce to the desired sharp-interface limit [35]. Numerical examples presented in the results section confirm that the non-variational multiphase-field formulation developed here yields phys-

ically realistic NW growth behaviors that can be quantitatively related to sharp-interface theory.

The evolution equations that incorporate the catalyst volume change and this localized driving force for crystallization can be written in the compact form

$$\tau \frac{\partial \phi_i}{\partial t} = -\frac{K(\vec{\phi})}{h} \frac{\hat{\delta}\tilde{F}}{\hat{\delta}\phi_i}, \quad (14)$$

with

$$\frac{\hat{\delta}\tilde{F}}{\hat{\delta}\phi_i} = \frac{\hat{\delta}F}{\hat{\delta}\phi_i} - \lambda_A h \frac{\partial g_l}{\partial \phi_i}, \quad (15)$$

which incorporates the change of catalyst volume, and

$$\frac{\hat{\delta}F}{\hat{\delta}\phi_1} = \frac{\delta F}{\delta\phi_1} - \Delta\mu\Omega_s^{-1}u(\phi_1, \phi_3), \quad (16)$$

$$\frac{\hat{\delta}F}{\hat{\delta}\phi_2} = \frac{\delta F}{\delta\phi_2}, \quad (17)$$

$$\frac{\hat{\delta}F}{\hat{\delta}\phi_3} = \frac{\delta F}{\delta\phi_3} + \Delta\mu\Omega_s^{-1}u(\phi_1, \phi_3), \quad (18)$$

which incorporate the driving force for crystallization only at the solid-liquid interface.

C. Lagrange multipliers and constraints

The equations above control the catalyst volume through the Lagrange multiplier λ_A but have not yet included the phase fraction condition $\sum_{i=1}^3 \phi_i = 1$. It has been shown previously [40] that such a condition is satisfied by writing the equations of motion as

$$\tau \frac{\partial \phi_i}{\partial t} = -\frac{K(\vec{\phi})}{h} \left(\frac{\hat{\delta}\tilde{F}}{\hat{\delta}\phi_i} - \frac{1}{3} \sum_{i=1}^3 \frac{\hat{\delta}\tilde{F}}{\hat{\delta}\phi_i} \right) \text{ for } i = 1, 2, \quad (19)$$

and

$$\phi_3 = 1 - \phi_1 - \phi_2. \quad (20)$$

The expression of the Lagrange multiplier λ_A derived in appendix A is given by

$$\lambda_A = \frac{\int Kh^{-1} \sum_{i=1}^2 \frac{\hat{\delta}F}{\hat{\delta}\phi_i} \frac{\partial \tilde{g}_l}{\partial \phi_i} dv - \frac{1}{3} \int Kh^{-1} \sum_{i=1}^2 \frac{\partial \tilde{g}_l}{\partial \phi_i} \sum_{j=1}^3 \frac{\hat{\delta}F}{\hat{\delta}\phi_j} dv + \dot{A}\tau}{\int K \sum_{i=1}^2 \left(\frac{\partial \tilde{g}_l}{\partial \phi_i} \right)^2 dv - \frac{1}{3} \int K \left(\sum_{i=1}^2 \frac{\partial \tilde{g}_l}{\partial \phi_i} \right)^2 dv}, \quad (21)$$

where \tilde{g}_l is a modified g_l function with ϕ_3 replaced by

$1 - \phi_1 - \phi_2$, and $\dot{A} \equiv dA/dt$ is related to the evolution of

the droplet concentration in the next subsection.

D. Droplet concentration evolution

The driving force $\Delta\mu$ at the solid-liquid interface generally depends on the over-saturation in the catalyst and the liquid-vapor interface curvature. To calculate the over-saturation part, a PF analog of Eq. 6 for the evolution of the number of growth atoms N_g in the catalyst needs to be included in the model. In terms of the PF variables, this evolution equation can be expressed as

$$\frac{dN_g}{dt} = \frac{J}{\eta} \int \phi_2 \phi_3 dv - \frac{1}{\Omega_s} \int \partial_t g_s(\vec{\phi}) dv, \quad (22)$$

where η in the first flux is a normalization constant with unit of length chosen such that $\eta^{-1} \int dv \phi_2 \phi_3 = \int_{lv} ds$ in the sharp-interface limit. Using a solid measuring function (similar to g_l in measuring liquid size)

$$g_s = \frac{\phi_1^2}{4} \{15(1 - \phi_1)[1 + \phi_1 - (\phi_3 - \phi_2)^2] + \phi_1(9\phi_1^2 - 5)\}, \quad (23)$$

time derivative of the g_s integral (the second term on the right-hand-side of Eq. 22) corresponds to the increasing rate of solid (i.e. the crystallization of Si atoms). During steady-state growth those two fluxes must balance each other. With $c_l = N_g/(N_c + N_g)$, the contribution of the over-saturation to the driving force is then given by $\beta(c_l - c_0)$, and the total driving force can be written as

$$\Delta\mu = -[\beta(c_l - c_0) - \lambda_A h \Omega_l], \quad (24)$$

where the first term is the over-saturation contribution and the second term is the Lagrange multiplier which can be reduced to the liquid-vapor curvature effect as shown later in the sharp-interface asymptotics. The droplet volume $A = \Omega_l N_g + A_c$ where A_c is the volume contribution of catalyst atoms assumed to remain constant. The rate of change of the volume in Eq. 21 is then given by

$$\dot{A} = \Omega_l \frac{dN_g}{dt}, \quad (25)$$

where dN_g/dt is given by Eq. 22. Also, at any time, the catalyst volume can be expressed as

$$A = A_0 \frac{1 - c_0}{1 - c_l}, \quad (26)$$

where A_0 is the catalyst size at $c_l = c_0$. In the limit of small supersaturation (c_l close to c_0), $A \approx A_0$.

E. Interface mobility

While the liquid-vapor interface relaxes rapidly to a shape with constant mean curvature, NW growth is a

comparatively much slower process controlled in different limits by the crystallization kinetics or the incorporation of Si atoms from the vapor phase. In addition, the evolution of the solid-vapor interface by surface diffusion is essentially frozen on the time scale of NW growth. Accordingly, the mobility function $K(\vec{\phi})$ should be chosen such that the solid-vapor interface mobility vanishes far from the triple junctions while the liquid-vapor interface mobility M_{lv} is much larger than the solid-liquid interface mobility M_{sl} . We use the form

$$K(\vec{\phi}) = (1 - 4\phi_1\phi_2)(1 + \alpha\phi_2\phi_3), \quad (27)$$

where α is chosen such that

$$\frac{\int_0^1 \phi_2(1 - \phi_2)\sqrt{1 + a_2\phi_2(1 - \phi_2)}d\phi_2}{\int_0^1 \phi_1(1 - \phi_1)\sqrt{1 + a_1\phi_1(1 - \phi_1)}K^{-1}d\phi_1} = M_{lv}/M_{sl}. \quad (28)$$

This integral condition will become clearer after we derive the sharp-interface limit of the PF equations.

F. Interface free-energy

The three binary interfaces involved in NW growth generally have different excess free-energy. The excess free-energy of the interface between phases where $\phi_j = 1$ and $\phi_k = 1$ is given by an integral of the free-energy density across the interface [40]

$$\gamma_{jk} = 2\sqrt{2}Wh \int_0^1 p(1 - p)\sqrt{1 + a_i p(1 - p)}dp, \quad (29)$$

where $W = \sqrt{\sigma/h}$, p is either ϕ_j or ϕ_k (since $\phi_j = 1 - \phi_k$ along the j-k interface) and a_i is the coefficient appearing in Eq. 10. This expression can be used to incorporate experimentally relevant surface energies for the solid-liquid, solid-vapor, and liquid-vapor interfaces into this model by using different coefficients a_i , a_j and a_k to vary the free-energy barriers between the j-k, i-k, and i-j phases, respectively. The expression above is limited to isotropic interfaces and the incorporation of crystalline anisotropy will be discussed later on.

G. Summary of phase-field model equations

We summarize here the PF model equations presented in the previous subsections. Even though some formulae are derived in the subsequent sharp-interface analysis, this self-contained summary is intended to facilitate the numerical implementation of the model. In the ST sharp-interface model, NW growth is governed by the growth law of Eq. 3 and the droplet concentration evolution of Eq. 6. In the PF model, the growth law is embodied in

Eqs. 19 and 20, which can be explicitly written as

$$\begin{aligned} \tau \frac{\partial \phi_1}{\partial t} &= K(\vec{\phi}) \left[W^2 \nabla^2 \phi_1 - 2\phi_1(1-\phi_1)(1-2\phi_1) \right. \\ &\quad \left. - \sum_{i=1}^3 \frac{\partial(a_i f_a^i + b_i f_b)}{\partial \phi_1} + \Delta \tilde{\mu} u(\phi_1, \phi_3) + \lambda_A \frac{\partial g_l}{\partial \phi_1} - \frac{1}{3} \lambda_\phi \right], \\ \tau \frac{\partial \phi_2}{\partial t} &= K(\vec{\phi}) \left[W^2 \nabla^2 \phi_2 - 2\phi_2(1-\phi_2)(1-2\phi_2) \right. \\ &\quad \left. - \sum_{i=1}^3 \frac{\partial(a_i f_a^i + b_i f_b)}{\partial \phi_2} + \lambda_A \frac{\partial g_l}{\partial \phi_2} - \frac{1}{3} \lambda_\phi \right], \end{aligned} \quad (31)$$

$$\phi_3 = 1 - \phi_1 - \phi_2, \quad (32)$$

with $u(\phi_1, \phi_3) = 15\phi_1^2\phi_3^2$,

$$\Delta \tilde{\mu} = \Delta \mu / (h\Omega_s), \quad (33)$$

$$\begin{aligned} \lambda_\phi &= \sum_{j=1}^3 \left[W^2 \nabla^2 \phi_j - 2\phi_j(1-\phi_j)(1-2\phi_j) \right. \\ &\quad \left. - \sum_{i=1}^3 \frac{\partial(a_i f_a^i + b_i f_b)}{\partial \phi_j} + \lambda_A \frac{\partial g_l}{\partial \phi_j} \right], \end{aligned} \quad (34)$$

and

$$\lambda_A = \frac{I_1 - I_2 + \dot{A}\tau}{I_3 - I_4}, \quad (35)$$

where

$$I_1 = \int K h^{-1} \sum_{i=1}^2 \frac{\hat{\delta} F}{\hat{\delta} \phi_i} \frac{\partial \tilde{g}_l}{\partial \phi_i} dv, \quad (36)$$

$$I_2 = \frac{1}{3} \int K h^{-1} \sum_{i=1}^2 \frac{\partial \tilde{g}_l}{\partial \phi_i} \sum_{j=1}^3 \frac{\hat{\delta} F}{\hat{\delta} \phi_j} dv, \quad (37)$$

$$I_3 = \int K \sum_{i=1}^2 \left(\frac{\partial \tilde{g}_l}{\partial \phi_i} \right)^2 dv, \quad (38)$$

$$I_4 = \frac{1}{3} \int K \left(\sum_{i=1}^2 \frac{\partial \tilde{g}_l}{\partial \phi_i} \right)^2 dv, \quad (39)$$

with $(\hat{\delta} F)/(\hat{\delta} \phi_i)$ defined by Eqs. 16, 17, and 18, and \tilde{g}_l obtained by replacing ϕ_3 with $1 - \phi_1 - \phi_2$ in Eq. 12. As we will see later in the sharp-interface analysis, the equations above can recover exactly the growth law in the

ST model (Eq.3). The droplet concentration evolution in the PF model is given by Eq.22

$$\frac{dN_g}{dt} = \frac{J}{\eta} \int \phi_2 \phi_3 dv - \frac{1}{\Omega_s} \int \partial_t g_s(\vec{\phi}) dv, \quad (40)$$

where J is the incorporation flux at the liquid-vapor interface, η is a constant with unit of length chosen such that $\eta^{-1} \int dv \phi_2 \phi_3$ gives the liquid-vapor surface area, g_s is the function given in Eq. 24. With this definition $\eta = \int dn \phi_2(n) \phi_3(n)$ where n is the coordinate normal to the liquid-vapor interface and ϕ_2 and $\phi_3 = 1 - \phi_2$ are the stationary one-dimensional phase-field profiles corresponding to an equilibrium interface. The value of η is given in the numerics section. In addition, $\Delta \tilde{\mu}$ is related to the Si atom concentration in the droplet $c_l = N_g/(N_c + N_g)$ and λ_A by

$$\Delta \tilde{\mu} = - \left[\frac{\beta(c_l - c_0)}{h\Omega_s} - \lambda_A \frac{\Omega_l}{\Omega_s} \right], \quad (41)$$

and the catalyst volume evolution is included by replacing \dot{A} in Eq. 35 with Eq. 25

$$\frac{dA}{dt} = \Omega_l \frac{dN_g}{dt}. \quad (42)$$

The interfacial free-energies are given by

$$\gamma_{sl} = 2\sqrt{2}Wh \int_0^1 p(1-p)\sqrt{1+a_2p(1-p)} dp, \quad (43)$$

$$\gamma_{sv} = 2\sqrt{2}Wh \int_0^1 p(1-p)\sqrt{1+a_3p(1-p)} dp, \quad (44)$$

$$\gamma_{lv} = 2\sqrt{2}Wh \int_0^1 p(1-p)\sqrt{1+a_1p(1-p)} dp. \quad (45)$$

The solid-liquid interface mobility is

$$M_{sl} = \frac{W^2}{\tau \gamma_{sl}}. \quad (46)$$

The last parameter we need to specify is related to the implicit assumption in the sharp-interface model that the liquid-vapor interface relaxes quasi-instantaneously to an equilibrium shape on the time scale of NW growth. This limit can be modeled by choosing α in the expression for the mobility

$$K(\vec{\phi}) = (1 - 4\phi_1\phi_2)(1 + \alpha\phi_2\phi_3), \quad (47)$$

such that the condition

$$\frac{\int_0^1 p(1-p)\sqrt{1+a_2p(1-p)} dp}{\int_0^1 p(1-p)\sqrt{1+a_1p(1-p)} K^{-1} dp} = \frac{M_{lv}}{M_{sl}} \gg 1 \quad (48)$$

is satisfied where $K = 1 + \alpha p(1-p)$ in the above expression where $K(\vec{\phi})$ is evaluated at the liquid-vapor interface with $\phi_1 = 0$, $\phi_2 = p$, and $\phi_3 = 1-p$, and the value of α is given in the numerical implementation part in section V.

H. Incorporation of crystalline anisotropy and facets

The incorporation of crystalline anisotropy in monophasic solidification models has been treated in various studies for atomically rough interfaces without [46, 47] and with [44] missing orientations as well as for faceted interfaces [41]. To incorporate the anisotropy of the solid-liquid interface excess free-energy in a multiphase system, an extension to the original Folch-Plapp model [40] needs to be developed. Because of the phase fraction condition $\sum_i \phi_i = 1$, incorporation of anisotropy through orientation-dependent gradient terms, as in monophasic solidification, is problematic. Therefore, we follow an alternate approach that consists of making the free-energy barrier height between the solid and liquid phases orientation-dependent. Details of this approach are given in appendix C and only the main results are summarized here. The functional derivatives are modified as

$$\frac{1}{h} \frac{\delta F}{\delta \phi_i} = \frac{\partial f_d^i}{\partial \phi_i} - W^2 \nabla^2 \phi_i + \sum_{l=1}^3 \left[a_l \frac{\partial f_a^l}{\partial \phi_i} + b_l \frac{\partial f_b}{\partial \phi_i} \right. \\ \left. + \frac{\partial}{\partial x} \left(\frac{\phi_{i,y}}{|\nabla \phi_i|^2} f_a^{l,i} \right) - \frac{\partial}{\partial y} \left(\frac{\phi_{i,x}}{|\nabla \phi_i|^2} f_a^{l,i} \right) \right], \quad (49)$$

with $\phi_{i,x} = \partial \phi_i / \partial x$. Anisotropy is introduced using the orientation-dependent coefficient

$$a_i(\theta) = \left[\frac{1}{2} a_i(\theta_j) + \frac{1}{2} a_i(\theta_k) \right], \quad (50)$$

where θ is the angle between the interface normal and a reference crystal axis, and

$$a_{l,i} = \frac{1}{2} \frac{\partial a_l(\theta_i)}{\partial \theta_i}. \quad (51)$$

Since the orientation angle of the j-k binary interface can be calculated by either

$$\sin \theta_j = -\partial_y \phi_j / \sqrt{(\partial_y \phi_j)^2 + (\partial_x \phi_j)^2}, \quad (52)$$

or

$$\sin \theta_k = -\partial_y \phi_k / \sqrt{(\partial_y \phi_k)^2 + (\partial_x \phi_k)^2}, \quad (53)$$

Eq. 50 combines the contribution from both θ_j and θ_k equally. To quantitatively incorporate an experimentally relevant anisotropic surface energy, the coefficient $a_i(\theta)$, which adjusts the height of the free-energy barrier between phases j and k, can be directly related to $\gamma_{jk}(\theta)$ by the relation derived in appendix C

$$a_i(\theta) = B_0 + B_1 \frac{\gamma_{jk}(\theta)}{Wh} + B_2 \left(\frac{\gamma_{jk}(\theta)}{Wh} \right)^2, \quad (54)$$

with $B_0 = -4.86349$, $B_1 = -0.693313$ and $B_2 = 23.3564$.

IV. SHARP-INTERFACE LIMIT OF PHASE-FIELD MODEL

In this section, we carry out an asymptotic analysis to relate the PF and sharp-interface models. In the present context, this analysis consists of deriving from the PF model the evolution equations for the solid-liquid and solid-vapor interfaces in the limit where the thickness of those spatially diffuse interfaces is small compared to the macroscopic scale of the system that is set by the NW radius, itself determined by the catalyst volume. The solid-vapor interface is assumed to have a vanishing mobility, consistent with the fact that surface diffusion is too slow to lead to a significant reconfiguration of this interface shape on the timescale of NW growth.

The present analysis is simpler than the thin interface limit of solidification models insofar as interface motion is not coupled to a long range diffusion field such as temperature [48] or alloy concentration [38, 40], i.e. the concentration of growth atom is assumed to be spatially uniform inside the catalyst. However, the analysis is made more complicated than the thin interface limit of solidification models by the introduction of a Lagrange multiplier λ_A to control the catalyst volume (Eq. 11). In order to first understand the effect of this Lagrange multiplier in the simplest possible two-phase configuration, we analyze in appendix B the shape evolution of an isolated liquid droplet in a vapor phase, which can be described by a single order parameter ϕ . We show that this evolution is governed in the sharp-interface limit by the equation

$$V = M \left(-\kappa \gamma + \gamma \frac{\int \kappa ds}{\int ds} + \frac{\dot{A}}{\int ds} \right), \quad (55)$$

where V is the normal interface velocity, M is an interface mobility, κ the is the interface curvature, s is the arclength coordinate along the interface such that $\int ds$, evaluated along the closed interface contour surrounding the droplet, represents the total interface length, and $\dot{A} = dA(t)/dt$ where $A(t)$ is the droplet area. Eq. 55 is simplest to interpret in the limit where the droplet area is constant ($\dot{A} = 0$). In this case, it implies that an arbitrarily shaped droplet will relax to a circle while preserving the droplet area since $\dot{A} = \int V ds = 0$. The motion involves both a local term $-M\kappa\gamma$, equivalent to motion by mean curvature, and an area-preserving non-local term $M\gamma \int \kappa ds / \int ds$. If $\dot{A} \neq 0$, Eq. 55 implies that relaxation to a circle will occur concurrently with a change of droplet area since $\int V ds = \dot{A}$ in this case.

In this section, we extend the sharp-interface analysis to the multiphase-field model, which describes the more complex three-phase configuration where different regions of the liquid droplet surface are in contact with the vapor and solid phases. In this case, Eq. 55 takes on a more complex form that couples the evolution of the solid-liquid and liquid-vapor interfaces to \dot{A} , which only vanishes in the steady-state growth regime. Importantly,

this evolution equation can be simplified and interpreted physically in the limit where the liquid-vapor interface mobility is much larger than the solid-liquid interface mobility. We show that, in this experimentally relevant limit where the droplet maintains a circular shape during growth, the Lagrange multiplier λ_A reduces to the term corresponding to the Laplace pressure inside the droplet in the sharp-interface model, and the desired evolution equation for the solid-liquid interface dynamics can be obtained by a suitable choice of driving force (chemical potential difference $\Delta\mu$) in the PF model.

To carry out the sharp-interface analysis, the essential equations in the PF model are reviewed here. The basic equations of motion (Eqs. 30 and 31) are

$$\begin{aligned} \tau \frac{\partial \phi_1}{\partial t} = & K(\vec{\phi}) \left[W^2 \nabla^2 \phi_1 - \frac{\partial f_p}{\partial \phi_1} \right. \\ & \left. + \Delta \tilde{\mu} u(\phi_1, \phi_3) + \lambda_A \frac{\partial g_l}{\partial \phi_1} - \frac{1}{3} \lambda_\phi \right], \end{aligned} \quad (56)$$

$$\tau \frac{\partial \phi_2}{\partial t} = K(\vec{\phi}) \left[W^2 \nabla^2 \phi_2 - \frac{\partial f_p}{\partial \phi_2} + \lambda_A \frac{\partial g_l}{\partial \phi_2} - \frac{1}{3} \lambda_\phi \right], \quad (57)$$

with

$$\Delta \tilde{\mu} = \Delta \mu / (h \Omega_s), \quad (58)$$

$$\lambda_\phi = \sum_{j=1}^3 \left[W^2 \nabla^2 \phi_j - \frac{\partial f_p}{\partial \phi_j} + \lambda_A \frac{\partial g_l}{\partial \phi_j} \right], \quad (59)$$

where we have used the expression of f_p in Eq. 10. The Lagrange multiplier λ_A is

$$\lambda_A = \frac{I_1 - I_2 + \dot{A}\tau}{I_3 - I_4}, \quad (60)$$

with the integrals $I_{1,2,3,4}$ defined in Eqs. 36-39.

At the liquid-vapor binary interface, Eqs. 56 and 57 are reduced to

$$\tau \frac{\partial \phi_1}{\partial t} = 0, \quad (61)$$

$$\tau \frac{\partial \phi_2}{\partial t} = K^{lv} \left(W^2 \nabla^2 \phi_2 - \frac{1}{2} \frac{\partial \tilde{f}_p^{lv}}{\partial \phi_2} + \frac{1}{2} \lambda_A \frac{\partial \tilde{g}_l}{\partial \phi_2} \right), \quad (62)$$

where \tilde{f}_p^{lv} and K^{lv} are f_p and $K(\vec{\phi})$ evaluated at the liquid-vapor interface ($\phi_1 = 0$, $\phi_3 = 1 - \phi_2$). The second term in the parenthesis on the right of Eq. 62 is obtained by summing the $\partial f_p / \partial \phi_2$ term in Eq. 57 with all the $\partial f_p / \partial \phi_i$ terms in λ_ϕ . The third term is obtained in the same way.

At the solid-liquid interface, the PF equations of motion become

$$\begin{aligned} \tau \frac{\partial \phi_1}{\partial t} = & K^{sl} \left[W^2 \nabla^2 \phi_1 - \frac{1}{2} \frac{\partial \tilde{f}_p^{sl}}{\partial \phi_1} \right. \\ & \left. - \frac{1}{2} \Delta \tilde{\mu} \frac{\partial \tilde{g}_l}{\partial \phi_1} + \frac{1}{2} \lambda_A \frac{\partial \tilde{g}_l}{\partial \phi_1} \right], \end{aligned} \quad (63)$$

$$\tau \frac{\partial \phi_2}{\partial t} = 0, \quad (64)$$

where \tilde{f}_p^{sl} and K^{sl} are f_p and $K(\vec{\phi})$ evaluated at the solid-liquid interface. For the $\Delta \tilde{\mu}$ term, $u(\phi_1, \phi_3)$ is reduced to $-\frac{1}{2} \frac{\partial \tilde{g}_l}{\partial \phi_1}$ at the solid-liquid interface. Other terms are obtained in the same way as in the liquid-vapor equation (Eq. 62).

The sharp-interface asymptotics of these equations can be taken directly from appendix B by matching the PF terms in Eqs. 62 and 63 to the single PF equation (Eq. B4) and taking the corresponding asymptotics from the single PF result (Eq. B20). For the solid-liquid interface, the sharp-interface equation is

$$v_{sl} = \frac{-\kappa_{sl}^0 \gamma_{sl}^0 + \frac{1}{2} (\lambda_A^1 - \Delta \tilde{\mu})}{Q_{sl}}, \quad (65)$$

with

$$\gamma_{sl}^0 = \int_{-\infty}^{+\infty} (\phi_{1,z_1}^0)^2 dz_1, \quad (66)$$

$$Q_{sl} = \int_{-\infty}^{+\infty} \alpha^{sl} (\phi_{1,z_1}^0)^2 dz_1. \quad (67)$$

Here, ϕ^0 is the equilibrium PF boundary profile, $\phi_{i,z}^0$ is the derivative of ϕ_i^0 with respect to z , $\alpha^{sl} = \tau D / (W^2 K^{sl})$, κ_{sl}^0 is the scaled solid-liquid interface curvature, λ_A^1 is the reduced Lagrange multiplier and the direction of interface normal coordinate z_1 points to the liquid phase (see appendix B for details). Similarly, the liquid-vapor equation is

$$v_{lv} = \frac{\kappa_{lv}^0 \gamma_{lv}^0 + \frac{1}{2} \lambda_A^1}{Q_{lv}}, \quad (68)$$

with

$$\gamma_{lv}^0 = \int_{-\infty}^{+\infty} (\phi_{2,z_2}^0)^2 dz_2, \quad (69)$$

$$Q_{lv} = \int_{-\infty}^{+\infty} \alpha^{lv} (\phi_{2,z_2}^0)^2 dz_2. \quad (70)$$

κ_{lv}^0 is the scaled liquid-vapor interface curvature, $\alpha^{lv} = \tau D / (W^2 K^{lv})$, and the direction of interface normal coordinate z_2 points to the liquid phase. Since this sharp-interface equation is based on the vapor phase ϕ_2 which

has a negative curvature in the NW growth geometry, the minus sign in front of the curvature term is removed to keep consistency with the positive curvature convention in the ST sharp-interface model.

By replacing v and κ^0 with their unscaled dimensional form $v = Vl_c/D$, $\kappa^0 = l_c\kappa$ for both the solid-liquid and the liquid-vapor interfaces, and using the dimensional interfacial energy γ (see appendix B), Eqs. 65 and 68 become

$$V_{sl} = M_{sl}(-\kappa_{sl}\gamma_{sl} + \lambda_A h - \Delta\mu\Omega_s^{-1}), \quad (71)$$

$$V_{lv} = M_{lv}(\kappa_{lv}\gamma_{lv} + \lambda_A h), \quad (72)$$

with the solid-liquid interface curvature κ_{sl} , the liquid-vapor curvature κ_{lv} and interfacial energies

$$\gamma_{lv} = 2Wh \int_{-\infty}^{+\infty} \left(\frac{\partial\phi_2^0}{\partial z_2} \right)^2 dz_2, \quad (73)$$

$$\gamma_{sl} = 2Wh \int_{-\infty}^{+\infty} \left(\frac{\partial\phi_1^0}{\partial z_1} \right)^2 dz_1. \quad (74)$$

These two interfacial energy equations are reduced to Eqs. 43 and 45 with the well-known equipartition relations $(\partial\phi_1^0/\partial z_1)^2 = \frac{1}{2}\tilde{f}_p^{sl}$ and $(\partial\phi_2^0/\partial z_2)^2 = \frac{1}{2}\tilde{f}_p^{lv}$, and the interface mobilities are given by

$$M_{lv} = \frac{W}{\tau h} \frac{1}{2 \int_{-\infty}^{+\infty} \left(\frac{\partial\phi_2^0}{\partial z_2} \right)^2 K_{lv}^{-1} dz_2}, \quad (75)$$

$$M_{sl} = \frac{W}{\tau h} \frac{1}{2 \int_{-\infty}^{+\infty} \left(\frac{\partial\phi_1^0}{\partial z_1} \right)^2 K_{sl}^{-1} dz_1}. \quad (76)$$

The result in Eq. 46 is obtained by substituting in the expression of K (Eq. 27) at a given binary interface into Eq. 76. The mobility ratio in Eq. 28 is also derived from here using the equipartition relations.

The sharp-interface counterpart of the Lagrange multiplier λ_A is derived following the procedure demonstrated in appendix B (Eqs. B23 - B26). The catalyst volume condition in Eq. A5 can be separated into two parts which cover the solid-liquid and liquid-vapor interfaces separately as the following

$$\begin{aligned} \dot{A} &= \int \sum_{i=1}^2 \left(\frac{\partial\tilde{g}_i}{\partial\phi_i} \frac{\partial\phi_i}{\partial t} \right) dv \\ &= \int_{sl} -V_{sl} \frac{\partial\tilde{g}_l}{\partial\phi_1} \frac{\partial\phi_1}{\partial z_1} ds dz_1 + \int_{lv} -V_{lv} \frac{\partial\tilde{g}_l}{\partial\phi_2} \frac{\partial\phi_2}{\partial z_2} ds dz_2. \end{aligned} \quad (77)$$

This is the multiphase-field equivalent of the single phase-field PF model in Eq. B25. Replacing the interface velocities in Eq. 78 with Eqs. 71 and 72 and solving for the Lagrange multiplier λ_A gives

$$\lambda_A h = \frac{\dot{A} - \gamma_{lv}\kappa_{lv}M_{lv}S_{lv} + (\gamma_{sl}\kappa_{sl} + \Delta\mu\Omega_s^{-1})M_{sl}S_{sl}}{M_{lv}S_{lv} + M_{sl}S_{sl}}, \quad (78)$$

which is the multiphase-field version of Eq. B26 with interface lengths S_{lv} and S_{sl} defined by

$$S_{lv} = \int_{lv} ds, \quad (79)$$

$$S_{sl} = \int_{sl} ds. \quad (80)$$

In addition, the solid-liquid and liquid-vapor interface curvatures are assumed to be constant in the derivation of Eq. 78.

Inserting Eq. 78 into Eqs. 71 and 72 gives the sharp-interface equations of motion for the solid-liquid and liquid-vapor interfaces

$$\begin{aligned} V_{sl} &= -M_{sl}\kappa_{sl}\gamma_{sl} - M_{sl}\Delta\mu\Omega_s^{-1} \\ &+ M_{sl} \frac{-\kappa_{lv}\gamma_{lv}M_{lv}S_{lv} + (\kappa_{sl}\gamma_{sl} + \Delta\mu\Omega_s^{-1})M_{sl}S_{sl} + \dot{A}}{M_{lv}S_{lv} + M_{sl}S_{sl}} \\ &= \frac{-\Delta\mu\Omega_s^{-1} - \kappa_{sl}\gamma_{sl} - \kappa_{lv}\gamma_{lv} + \frac{\dot{A}}{M_{lv}S_{lv}}}{\left(\frac{1}{M_{sl}} + \frac{S_{sl}}{S_{lv}} \frac{1}{M_{lv}} \right)}. \end{aligned} \quad (81)$$

$$\begin{aligned} V_{lv} &= M_{lv}\kappa_{lv}\gamma_{lv} \\ &+ M_{lv} \frac{-\kappa_{lv}\gamma_{lv}M_{lv}S_{lv} + (\kappa_{sl}\gamma_{sl} + \Delta\mu\Omega_s^{-1})M_{sl}S_{sl} + \dot{A}}{M_{lv}S_{lv} + M_{sl}S_{sl}} \\ &= \frac{\Delta\mu\Omega_s^{-1} + \kappa_{sl}\gamma_{sl} + \kappa_{lv}\gamma_{lv} + \frac{\dot{A}}{M_{sl}S_{sl}}}{\left(\frac{S_{lv}}{S_{sl}} \frac{1}{M_{sl}} + \frac{1}{M_{lv}} \right)}. \end{aligned} \quad (82)$$

These expressions can be further simplified in the limit $M_{lv} \gg M_{sl}$ where the liquid droplet relaxes quasi-instantaneously to an equilibrium shape during growth. Neglecting the volume change contribution \dot{A} , which is typically small and vanishes in the steady-state growth regime, Eq. 78 reduces in this limit to

$$\lambda_A h \approx -\kappa_{lv}\gamma_{lv}, \quad (83)$$

which corresponds to the Laplace pressure of the droplet. The sharp-interface limit of the solid-liquid interface motion becomes

$$v_n = V_{sl} = M_{sl}(-\kappa_{sl}\gamma_{sl} - \frac{\Delta\mu}{\Omega_s} - \kappa_{lv}\gamma_{lv}). \quad (84)$$

We note that, with the volume change factor \dot{A} included, the expression for the Lagrange multiplier contains an additional contribution

$$\lambda_A h \approx \frac{\dot{A}}{M_{lv}S_{lv}} - \kappa_{lv}\gamma_{lv}. \quad (85)$$

However, the same solid-liquid interface equation of motion (Eq. 84) is obtained since \dot{A} represents a high order contribution in the limit where $M_{sl}/M_{lv} \ll 1$. As a result, the rapid volume change mediated by the motion of the liquid-vapor interface has a negligibly small effect on the NW growth rate in this limit, as physically desired.

Finally, Eq. 84 can be readily seen to have the same form as the equation for the normal velocity of the solid-liquid interface in the sharp-interface model, which is obtained by combining Eqs. 3-5

$$v_n = M_{sl} \left[\frac{\beta(c_l - c_0)}{\Omega_s} + \kappa_{lv}\gamma_{lv} \frac{\Omega_l}{\Omega_s} - \kappa_{sl}\gamma_{sl} - \kappa_{lv}\gamma_{lv} \right], \quad (86)$$

if $\Delta\mu$ is chosen in the PF model as

$$\begin{aligned} \Delta\mu &= -[\beta(c_l - c_0) + \kappa_{lv}\gamma_{lv}\Omega_l] \\ &= -[\beta(c_l - c_0) - \lambda_A h \Omega_l], \end{aligned} \quad (87)$$

where Eq. 83 is used in the second equality. By the same argument given above, this $\Delta\mu$ expression remains valid when $\dot{A} \neq 0$ since the slow catalyst volume change has a negligible effect on the solid-liquid interface dynamics in the rapid droplet-shape relaxation limit $M_{sl}/M_{lv} \ll 1$.

V. NUMERICAL EXAMPLES AND COMPARISON WITH SHARP-INTERFACE THEORY

In this section, we discuss the numerical implementation of the phase-field model. We then present results of simulations that illustrate the ability of the model to reproduce basic features of NW growth. We consider first the simpler case of an isotropic solid-liquid interface and then consider the more realistic case of a faceted solid-liquid interface. The quantitative validity of the approach is tested by comparisons with sharp-interface theory for the NW growth shape and velocity.

A. Numerical implementation

The PF equations are first written in dimensionless form by introducing the dimensionless time $\bar{t} = t/\tau$ and dimensionless length $\bar{x} = x/W$ as well as the corresponding dimensionless derivative operator $\bar{\nabla} = W\nabla$, volume element $d\bar{v} = dv/W^2$, and catalyst size $\bar{A} = A/W^2$. The functional derivatives that include the driving force for crystallization become

$$\begin{aligned} \frac{1}{h} \frac{\delta F}{\delta \phi_1} &= - \left[\bar{\nabla}^2 \phi_1 - 2\phi_1(1 - \phi_1)(1 - 2\phi_1) \right. \\ &\quad \left. - \sum_{i=1}^3 \frac{\partial(a_i f_a^i + b_i f_b)}{\partial \phi_1} + \Delta \tilde{\mu} u(\phi_1, \phi_3) \right], \end{aligned} \quad (88)$$

$$\begin{aligned} \frac{1}{h} \frac{\delta F}{\delta \phi_2} &= - \left[\bar{\nabla}^2 \phi_2 - 2\phi_2(1 - \phi_2)(1 - 2\phi_2) \right. \\ &\quad \left. - \sum_{i=1}^3 \frac{\partial(a_i f_a^i + b_i f_b)}{\partial \phi_2} \right], \end{aligned} \quad (89)$$

$$\begin{aligned} \frac{1}{h} \frac{\delta F}{\delta \phi_3} &= - \left[\bar{\nabla}^2 \phi_3 - 2\phi_3(1 - \phi_3)(1 - 2\phi_3) \right. \\ &\quad \left. - \sum_{i=1}^3 \frac{\partial(a_i f_a^i + b_i f_b)}{\partial \phi_3} - \Delta \tilde{\mu} u(\phi_1, \phi_3) \right], \end{aligned} \quad (90)$$

with

$$\Delta \tilde{\mu} = - \left[\frac{\beta}{h \Omega_s} (c_l - c_0) - \lambda_A \frac{\Omega_l}{\Omega_s} \right]. \quad (91)$$

Using Eqs. 88-90, the Lagrange multiplier λ_A can be evaluated as

$$\lambda_A = \frac{I_1 - I_2 + \frac{\partial \bar{A}}{\partial \bar{t}}}{I_3 - I_4}, \quad (92)$$

where

$$I_1 = \int K h^{-1} \sum_{i=1}^2 \frac{\delta F}{\delta \phi_i} \frac{\partial \tilde{g}_i}{\partial \phi_i} d\bar{v}, \quad (93)$$

$$I_2 = \frac{1}{3} \int K h^{-1} \sum_{i=1}^2 \frac{\partial \tilde{g}_i}{\partial \phi_i} \sum_{j=1}^3 \frac{\delta F}{\delta \phi_j} d\bar{v}, \quad (94)$$

$$I_3 = \int K \sum_{i=1}^2 \left(\frac{\partial \tilde{g}_i}{\partial \phi_i} \right)^2 d\bar{v}, \quad (95)$$

$$I_4 = \frac{1}{3} \int K \left(\sum_{i=1}^2 \frac{\partial \tilde{g}_i}{\partial \phi_i} \right)^2 d\bar{v}. \quad (96)$$

The phase-field evolution equations are

$$\frac{\partial \phi_j}{\partial \bar{t}} = - \frac{K(\vec{\phi})}{h} \left(\frac{\delta \tilde{F}}{\delta \phi_j} - \frac{1}{3} \sum_{i=1}^3 \frac{\delta \tilde{F}}{\delta \phi_i} \right), \quad (97)$$

for $j=1$ and 2 with

$$\frac{1}{h} \frac{\delta \tilde{F}}{\delta \phi_i} = \frac{1}{h} \frac{\delta F}{\delta \phi_i} - \lambda_A \frac{\partial g_l}{\partial \phi_i}, \quad (98)$$

and

$$\phi_3 = 1 - \phi_1 - \phi_2. \quad (99)$$

The evolution equations for the catalyst concentration $c_l = (N_c + N_g)/N_c$ and catalyst volume (area in 2D) are determined by

$$\frac{dN_g}{dt} = \frac{JW\tau}{\bar{\eta}} \int \phi_2 \phi_3 d\bar{v} - \frac{W^2}{\Omega_s} \int \frac{\partial g_s}{\partial \bar{t}} d\bar{v}, \quad (100)$$

which determines the evolution of c_l at fixed number of catalyst atoms N_c , and

$$\frac{d\bar{A}}{d\bar{t}} = \frac{\Omega_l}{W^2} \frac{dN_g}{d\bar{t}}, \quad (101)$$

respectively, where $\bar{\eta} = \eta/W$ and in 2D the incorporation flux J has the unit of atoms per length per time.

To model an anisotropic surface energy, the $\frac{\partial(a_i f_a^i + b_i f_b)}{\partial \phi_j}$ term in Eqs. 88-90 is replaced by the form defined by Eq. 49

$$\begin{aligned} \sum_{i=1}^3 \frac{\partial(a_i f_a^i + b_i f_b)}{\partial \phi_j} \rightarrow \\ \sum_{i=1}^3 \left[a_i \frac{\partial f_a^i}{\partial \phi_j} + b_i \frac{\partial f_b}{\partial \phi_j} + \frac{\partial}{\partial x} \left(\frac{\phi_{j,y}}{|\nabla \phi_j|^2} f_a^i a_{i,j} \right) \right. \\ \left. - \frac{\partial}{\partial y} \left(\frac{\phi_{j,x}}{|\nabla \phi_j|^2} f_a^i a_{i,j} \right) \right]. \end{aligned} \quad (102)$$

The constant barrier parameter a_i in the isotropic model becomes orientation dependent $a_i(\theta)$ in the anisotropic model. The orientation dependent barrier parameter a_i and its derivative $a_{i,j}$ are defined in Eqs. 50 and 51. To model a given anisotropic solid-liquid interfacial energy $\gamma(\theta)$, $a_i(\theta)$ needs to be calculated numerically using Eq. C9.

The phase-field evolution equations (Eq. 97) are stepped forward in time with an explicit Euler scheme with centered finite difference approximations of the spatial derivatives. The evolution equations for the concentration (Eq. 100) and catalyst volume (Eq. 101) are also stepped forward in time with an explicit Euler scheme with parameters $c_0 = 0.45$, $\beta \Omega_s^{-1} h^{-1} = 2.0$ and $\Omega_s/W^2 = \Omega_l/W^2 = 1.0$ unless explicitly specified otherwise. Space and time discretizations are chosen to be $\Delta x/W = \Delta y/W = 0.4$ and $\Delta t/\tau = 0.001$. To keep the numerics tractable, we use a mobility ratio $M_{lv}/M_{sl} \approx 20$, corresponding to $\alpha \approx 110$ in the expression of $K(\vec{\phi})$ (Eq. 47), which is sufficiently large for the liquid-vapor interface to relax to a circular equilibrium shape on the characteristic time scale of NW growth. The liquid-vapor surface energy is isotropic and given by $a_1 = 0$. The scaling factor in Eq. 100 $\bar{\eta} = 0.71$. The other two surface energy parameters (a_2 and a_3) are computed using Eq. C9 to match desired ratios of interfacial free-energies. The parameter b_i in the potential function f_p is set to 80 to reduce the triple junction size. To increase performance, only grid points near the liquid phase are computed.

B. From droplet to nanowire

Here we first demonstrate some basic features of this PF NW growth model based on isotropic interfacial free-energies. For the silicon-gold system, we use the values $\gamma_{sv} = 1.2 \text{ Jm}^{-2}$, $\gamma_{sl} = 0.8 \text{ Jm}^{-2}$ and $\gamma_{lv} = 1.0 \text{ Jm}^{-2}$ which are similar to those given in previous studies [16]. The initial configuration is a substrate-vapor system. By seeding a catalyst droplet of a specified volume on the substrate with $c_l = c_0$, without Si incorporation at the

liquid-vapor interface, the catalyst relaxes to an equilibrium shape given by Young's condition. Once the flux of Si atom is switched on at the liquid-vapor interface, the NW grows vertically as demonstrated in Fig. 3.

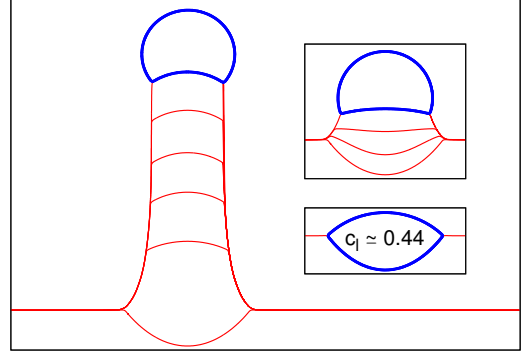


FIG. 3. PF simulation with isotropic interfaces illustrating the evolution from droplet to NW. The solid-liquid and solid-vapor interfaces are shown as red lines at different times and the solid-liquid and liquid-vapor interfaces bounding the catalyst droplet are only shown together for clarity as a thicker blue line at the latest time. The top right inset shows interfaces more closely spaced in time during the initial growth stage. Simulation parameters are $A_0/W^2 = 313$, $JW\tau = 0.007$. The lower right inset shows the equilibrium configuration on the substrate before growth ($J = 0$).

The catalyst concentration and volume during growth are shown in Fig. 4 and Fig. 5, respectively. The catalyst is under-saturated at the start of growth due to the Gibbs-Thompson effect associated with the curvature of the liquid-vapor surface and becomes over-saturated as growth atoms become incorporated in the catalyst droplet. Finally, the growth velocity and droplet concentration reach constant values during steady-state growth. For a given catalyst size, the volume evolution described by Eq. 25 is also accurately reproduced as shown in Fig. 5.

C. Nanowire radius for steady-state growth

We now compare the steady-state NW growth shape to the prediction of sharp-interface theory. The steady-state NW radius predicted by sharp-interface theory, denoted here as R_{si} , is determined by the three interfacial free-energies together with the size of the catalyst (as shown in Fig. 6). For isotropic interfaces, the Young-Herring condition reduces to Young's condition at the triple-phase junction. For a vertical sidewall, the projection of the capillary forces on the vertical and horizontal directions yield the relations

$$\gamma_{sv} = \gamma_{sl} \sin \theta_1 + \gamma_{lv} \sin \theta_2, \quad (103)$$

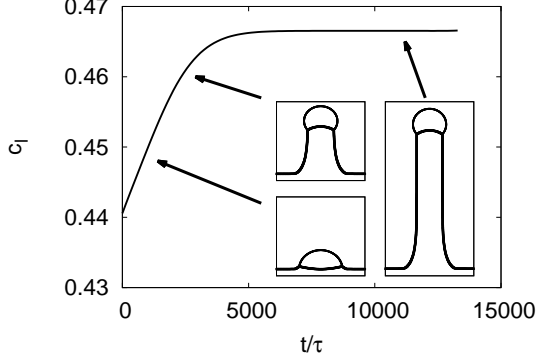


FIG. 4. Droplet concentration versus time scaled by the phase-field relaxation time τ during NW growth for the same parameters as Fig. 3. Insets show morphologies during initial growth, tapering, and steady-state growth.

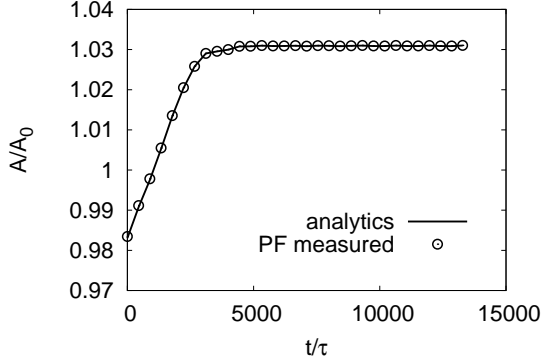


FIG. 5. Catalyst area A scaled by the area of an equilibrium droplet A_0 before growth versus dimensionless time t/τ with A analytically predicted by Eq. 26 with c_l from the PF simulation of Fig. 4 (solid line) and with A computed from the same simulation using $\int g_l(\vec{\phi}) dv$ that defines the catalyst area in Eq. 11 (open circles). Simulation parameters are the same as in Fig. 3 and Fig. 4.

and

$$\gamma_{sl} \cos \theta_1 = \gamma_{lv} \cos \theta_2, \quad (104)$$

respectively.

The radius of curvature of the solid-liquid (R_1) and the liquid-vapor (R_2) interfaces are related to the NW radius R_{si} by

$$R_1 = R_{si} / \sin \theta_1, R_2 = R_{si} / \sin \theta_2, \quad (105)$$

from which we obtain the expression for the catalyst area

$$A = \pi R_2^2 - \theta_2 R_2^2 + R_2^2 \sin \theta_2 \cos \theta_2 - \theta_1 R_1^2 + R_1^2 \sin \theta_1 \cos \theta_1. \quad (106)$$

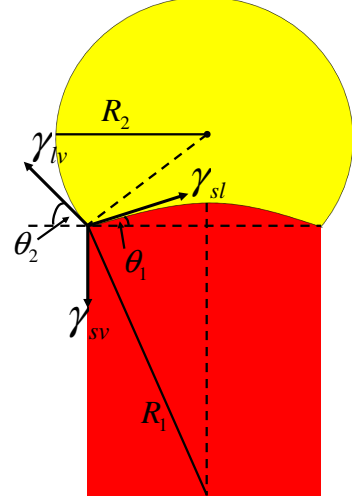


FIG. 6. Definition of geometrical parameters used to characterize steady-state NW growth. The NW (red region) and droplet catalyst (yellow region) are shown together with the radius of curvature of the solid-liquid (liquid-vapor) interface R_1 (R_2), the excess free-energies for the solid-liquid (γ_{sl}), liquid-vapor (γ_{lv}), and solid-vapor (γ_{sv}) interfaces, and the corresponding dihedral angles determined by Young's condition at the three-phase junction, which are defined here as the angle between a horizontal line and the solid-liquid interface (θ_1) and the liquid-vapor interface (θ_2).

This expression can be further reduced to

$$A^{1/2} = R_{si} \left(\frac{\pi - \theta_2}{\sin^2 \theta_2} - \frac{\theta_1}{\sin^2 \theta_1} + \cot \theta_1 + \cot \theta_2 \right)^{1/2}, \quad (107)$$

which predicts that the sharp-interface NW radius R_{si} is proportional to the square root of the catalyst area. As shown in Fig. 7, this prediction is in very good quantitative agreement with PF simulations where the catalyst area was varied over a very broad range.

D. Steady-state nanowire growth rate

The dependence of the NW growth rate on radius has been extensively studied experimentally [5, 13–15]. Both size-dependent and size-independent growth rates have been reported in different experimental settings. In this section, we examine the convergence of the NW growth rate in the PF model to its sharp-interface asymptotics. We consider two physically distinct growth regimes. The first is the one where growth is limited by the solid-liquid interface kinetics and the chemical potential of growth atoms can be assumed to be equal in the liquid and vapor

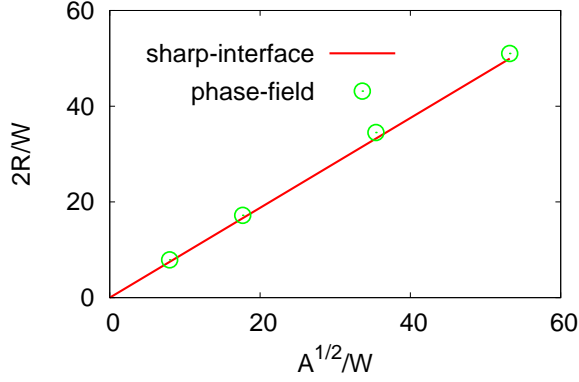


FIG. 7. NW diameter $2R$ normalized by the interface thickness W versus dimensionless catalyst size defined as $A^{1/2}/W$ where A is the steady-state value of the catalyst area. The analytical prediction of the sharp-interface model (Eq. 107 and red line) is compared to the results of PF simulations (open green circles). A constant flux $JW\tau = 0.0014$ is used and other parameters are the same as in Fig. 3.

and constant in time, i.e. those two phases equilibrate quickly on the time scale where the solid adds one additional layer of atoms. In this regime, the growth rate depends on catalyst size. The second is the one considered by ST where the NW growth rate is limited by the incorporation rate of growth atoms at the droplet surface. Since the total number of incorporated Si atoms is proportional to the droplet surface area which is geometrically related to NW radius, the growth rate in this case becomes size-independent and is controlled only by the droplet incorporation rate.

For the first interface-kinetics-dominated regime, the growth rate is determined by Eq. 84 derived in the sharp-interface analysis of our PF model (section. IV) with a constant $\Delta\mu$. This equation implies that the NW growth rate vanishes at a critical driving force $\Delta\mu^* = -(\kappa_{sl}\gamma_{sl} + \kappa_{lv}\gamma_{lv})\Omega_s$. Using Eq. 105 for the radii of curvature and Eq. 103, this critical driving force can be simplified to

$$\Delta\mu^* = -\gamma_{sv}\Omega_s/R_{si}. \quad (108)$$

With a given $\Delta\mu$, the growth rate is then proportional to $\Delta\mu^* - \Delta\mu$. Such a growth law can be easily tested in our PF model by carrying out simulations that run long enough to reach the steady-state growth regime with $\Delta\mu$ held constant. Since the concentration dynamics described in Eqs. 22, 24 and 25 is not needed in these constant $\Delta\mu$ simulations, catalyst volumes are set to $A = A_0$. PF simulation results shown in Fig. 8 confirm the predicted linear dependence of the NW growth rate on $\Delta\mu^* - \Delta\mu$.

NWs of different size are then grown using this model in the interface-kinetics-dominated regime by seeding the growth with different catalyst sizes. Since the critical

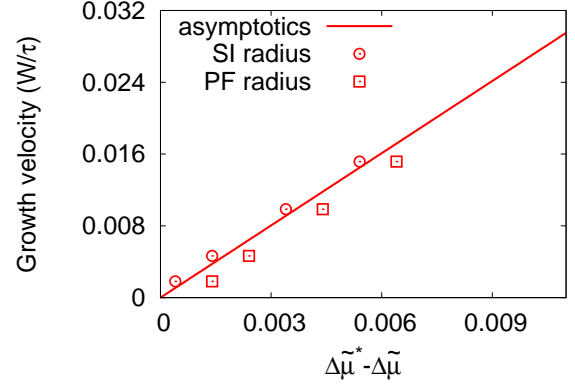


FIG. 8. Comparison of steady-state NW growth rate versus driving force in PF simulations and predicted by sharp-interface theory for an initial catalyst area $A_0 = 1254 W^2$. By calculating the critical driving force using Eq. 108, the growth rate (Eq. 84) is well-reproduced in PF simulations as shown by sharp-interface (SI) radius data points. This comparison is very sensitive to the NW radius. The growth rate computed by replacing R_{si} in Eq. 108 by the slightly different PF radius shown in Fig. 7 (PF radius points) produces a noticeable shift of the growth threshold.

driving force for NW growth depends on the solid-liquid and liquid-vapor curvatures, the growth rate becomes size-dependent as shown in Fig. 9.

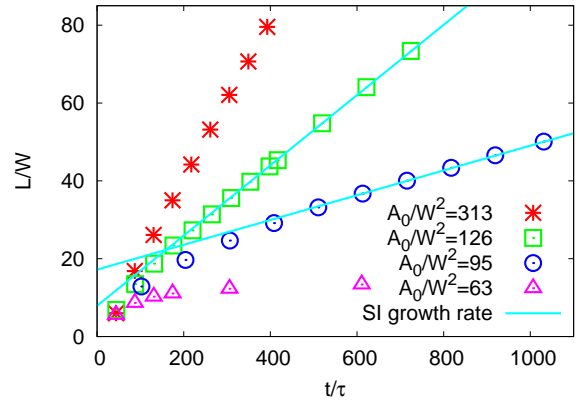


FIG. 9. Scaled NW growth length as a function of scaled time for different catalyst sizes in the interface-kinetics-dominated regime where the droplet chemical potential is held constant (here $\Delta\tilde{\mu} = -0.14$) instead of being determined by Eqs. 22, 24, and 25. The results of PF simulations (symbols) agree well with the prediction of sharp-interface (SI) theory based on Eq. 84 (lines).

For the second incorporation-rate-dominated regime, a simple relation between the steady-state NW growth rate V and the incorporation flux J can be derived from the wire geometry shown in Fig. 6 and the flux balance

condition (Eq. 6)

$$V = J\Omega_s \frac{\pi - \theta_2}{\sin \theta_2}, \quad (109)$$

The PF results agrees well with the prediction in Eq. 109 as shown in Fig. 10. Eq. 109 can also be used to calculate

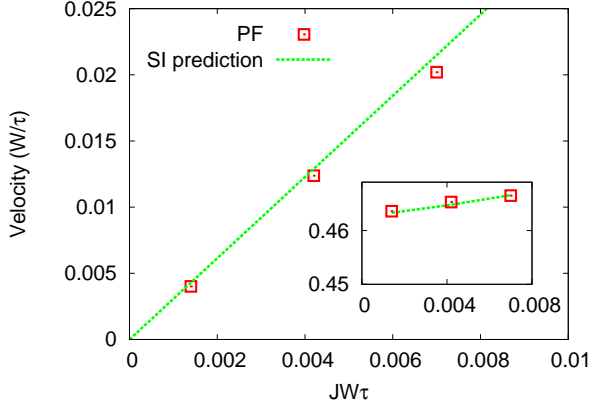


FIG. 10. Comparison of the PF steady-state growth rate with the sharp-interface prediction (Eq. 109). The inset is a comparison of the PF steady-state catalyst concentration with the sharp-interface prediction (Eq. 110). The catalyst size is $A_0/W^2 = 313$.

the steady-state concentration in the catalyst droplet by equating the growth velocity in Eq. 109 to the sharp-interface velocity in Eq. 86. Assuming $\Omega_l = \Omega_s$ and using the solid-liquid interface mobility in Eq. 46 together with Eq. 105, the catalyst concentration is related to the sharp-interface NW radius R_{si} by

$$\beta(c_l - c_0) = J \frac{\gamma_{sl} \tau \Omega_s^2}{W^2} \frac{\pi - \theta_2}{\sin \theta_2} + \Omega_s \frac{\gamma_{sl} \sin \theta_1}{R_{si}}. \quad (110)$$

Combining Eq. 110 with the radius-volume relation in Eq. 107 and the volume-concentration relation in Eq. 26, one can predict the catalyst concentration as a function of the incorporation flux J as shown in the inset of Fig. 10.

NWs of different size are also grown in this incorporation-rate-dominated regime using the full N_g dynamics described in Eqs. 22, 24 and 25. Since the number of incorporated growth atoms into the droplet is the product of the droplet surface area and a constant current density J , the rate of incorporation of growth atoms into the solid scales as the product of the NW growth rate V and solid-liquid interface area divided by the atomic volume of solid Ω_s . Both the droplet surface area and solid-interface area scale as R^{d-1} (where d is the spatial dimension), and $V \sim J\Omega_s$ becomes independent of the NW radius in this limit, as shown in our numerical results in Fig. 11.

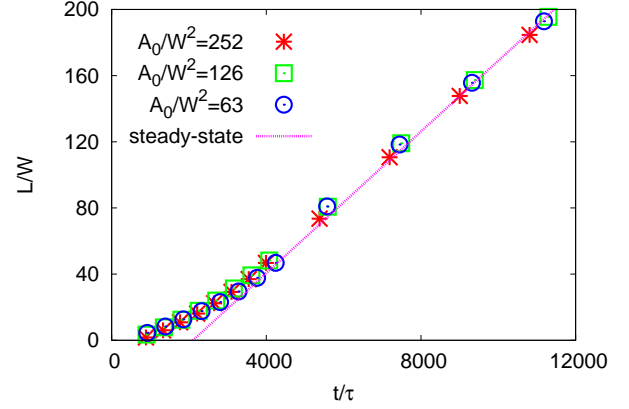


FIG. 11. NW length L as a function of time for different catalyst sizes in the incorporation-rate-dominated regime. Other parameters are the same as in Fig. 3. The steady-state line is based on predicted growth rate from Eq. 109.

E. Faceted nanowire growth

In this part we present results for faceted NW growth based on the anisotropic PF model introduced in section III H. For simplicity, we consider a solid-liquid anisotropy with γ -plot of the form

$$\gamma_{sl}(\theta) = \gamma_{sl}^0 \frac{1 + \delta_a |\sin 2\theta| + \delta_b |\cos 2\theta|}{1 + \min(\delta_a, \delta_b)}, \quad (111)$$

which has cusps at orientations $\theta = 0, \pm\pi/2, \pi$ and $\theta = \pm\pi/4, \pm3\pi/4$ corresponding to (10) and (11) facets, respectively. Similar γ -plot has been measured experimentally for Si [49] and computed for the Si-Au system by atomistic simulations [29]. For the liquid-vapor and the solid-vapor interfaces, we use isotropic form $\gamma_{lv} = \gamma_{lv}^0$ and $\gamma_{sv} = \gamma_{sv}^0$.

To make $\gamma_{sl}(\theta)$ differentiable, we round the cusps by replacing the absolute value function $|x|$ by a smooth function $\sqrt{\epsilon^2 + x^2}$, which transforms Eq. 111 into a regularized form

$$\gamma_{sl}(\theta) = \gamma_{sl}^0 \frac{1 + \delta_a \sqrt{\sin^2 2\theta + \epsilon^2} + \delta_b \sqrt{\cos^2 2\theta + \epsilon^2}}{1 + \min(\delta_a, \delta_b)}. \quad (112)$$

This form is implemented in the PF model using the procedure outlined in section III H and further detailed in appendix C. Simulations are carried out with $\gamma_{sv}^0 = 1.2 \text{ Jm}^{-2}$, $\gamma_{lv}^0 = 1.0 \text{ Jm}^{-2}$, $\gamma_{sl}^0 = 0.8 \text{ Jm}^{-2}$, and $\epsilon = 0.01$.

In principle, the anisotropy parameters δ_a and δ_b can be varied independently. For some regions of the (δ_a, δ_b) parameter space, the solid-liquid interface stiffness $\gamma_{sl} + d^2\gamma_{sl}/d\theta^2$ becomes negative over a range of θ corresponding to thermodynamically unstable orientations that are excluded from the equilibrium crystal shape. Those so-called “missing orientations”, defined by $\gamma_{sl} + d^2\gamma_{sl}/d\theta^2 < 0$, are completely unrelated to faceted

orientations that, in contrast, correspond to large positive extremal values of the stiffness in the regularized γ -plot of the form of Eq. 112. A γ -plot, such as the one considered here and other more general forms, can generally yield equilibrium shapes with missing orientations and no facets, no missing orientations and facets, or a mix of both facets and missing orientations. While various methods have been developed to handle missing orientations in the PF model [44, 45], we restrict our attention here to a region of the (δ_a, δ_b) parameter space that yields solid-liquid equilibrium shapes without missing orientations. For this purpose, we choose to constrain δ_a and δ_b by the relation $3\delta_a = \sqrt{1 - 9\delta_b^2}$, which is obtained by requiring that the minimum value of the stiffness over all angles equals zero, and hence that the stiffness is always equal to zero or positive for $0 \leq \theta \leq 2\pi$. For $\delta_a = \delta_b = \sqrt{2}/6$, the equilibrium shape is octagonal and completely faceted with (10) and (11) facets of equal lengths in the $\epsilon \rightarrow 0$ limit, while for $\delta_a \neq \delta_b$, the equilibrium shape consists of facets of unequal lengths and rough parts with finite positive stiffness. In the latter case, (10) facets have lower energy and are longer than (11) facets in the equilibrium shape for $\delta_a > \delta_b$ and vice versa for $\delta_a < \delta_b$.

Examples of NW growth from a (10) substrate are shown in Fig. 12. When (10) facets are energetically favored ($\delta_a > \delta_b$), simulations reproduce the standard mode of tapered growth normal to the substrate (Fig. 12a). In contrast, when (11) facets are energetically favored ($\delta_a < \delta_b$), growth normal to the substrate becomes unstable. For large enough flux of growth atoms (measured in our 2D simulations by the dimensionless product $JW\tau$), the NW first emerges normal to the substrate but then kinks towards another direction after a finite growth distance, which corresponds to (11) in the example of Fig. 12b. In contrast, for small flux, the NW is not able to emerge from the substrate before kinking and instead crawls along the substrate as seen in Fig. 12c.

Those simulations illustrate that NW growth is controlled by a subtle balance of interface energetics and growth kinetics. A more exhaustive study of NW growth behavior as a function of the interface anisotropy parameters space, including solid-vapor anisotropy that has been neglected here for simplicity, will be presented elsewhere. In the rest of this section, we focus on comparing the faceted NW tip shape obtained in phase-field simulations to the one predicted by sharp-interface theory. For this purpose, we focus on the case $\delta_a = \delta_b$ that yields a completely faceted octagonal solid-liquid equilibrium crystal shape with (10) and (11) facets of equal energies and equal lengths. However, during NW growth from a (10) substrate, the side facets (i.e. (11) and (11) facets) are truncated to a shorter length than the main (10) facet, as illustrated by the phase-field simulation in Fig. 13. This raises the question of how to predict the length of truncated facets in the NW growth geometry. Before addressing this question, we note that in the simulation

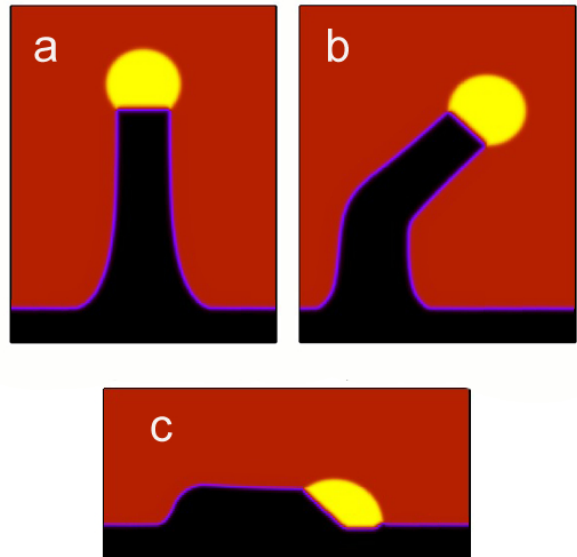


FIG. 12. NW morphologies. Three phases are colored as red (vapor), yellow (liquid) and black (solid). Catalyst size is $A_0/W^2 = 1254$. In (a), $\delta_a = 0.3179, \delta_b = 0.1, JW\tau = 0.0035$. In (b), $\delta_a = 0.1, \delta_b = 0.3179, JW\tau = 0.0035$. In (c), $\delta_a = 0.1, \delta_b = 0.3179, JW\tau = 0.0007$.

of Fig. 13, growth normal to the substrate is unstable with isotropic solid-vapor interface. Normal growth was therefore enforced by imposing zero flux boundary conditions on all phase fields about a vertical axis that splits the NW into two equal mirror symmetric parts. As will be described elsewhere, normal growth can also be obtained in a more physical way without imposing mirror symmetry by making the solid-vapor interface faceted, with facets modeled with a similar form of γ -plot as Eq. 112. However, the simulation of Fig. 13 suffices for the purpose of comparing the steady-state NW growth shape to the prediction of sharp-interface theory.

The first approach is to apply the geometrical Wulff construction of the equilibrium crystal shape. The latter can be expressed in an equivalent parametric representation where the cartesian coordinates of the interface are functions of θ given by [50]

$$x(\theta) = \tilde{\gamma}_{sl}(\theta) \sin \theta + \tilde{\gamma}'_{sl}(\theta) \cos \theta \quad (113)$$

$$y(\theta) = \tilde{\gamma}_{sl}(\theta) \cos \theta - \tilde{\gamma}'_{sl}(\theta) \sin \theta, \quad (114)$$

where we have defined the dimensionless solid-liquid interface energy $\tilde{\gamma}_{sl}(\theta) = \gamma_{sl}(\theta)/\gamma_{lv}^0$. Here x and y are taken to be dimensionless since the entire NW shape scales proportionally to the NW diameter itself $\sim \sqrt{A}$. This parametric representation is obtained as a solution of the equilibrium Gibbs-Thomson condition

$$[\tilde{\gamma}_{sl}(\theta) + \tilde{\gamma}''_{sl}(\theta)] \kappa(\theta) = C, \quad (115)$$

where $\kappa(\theta)$ is the interface curvature and C is constant. Eqs. 113 and 114 over the interval $0 \leq \theta \leq 2\pi$ define the

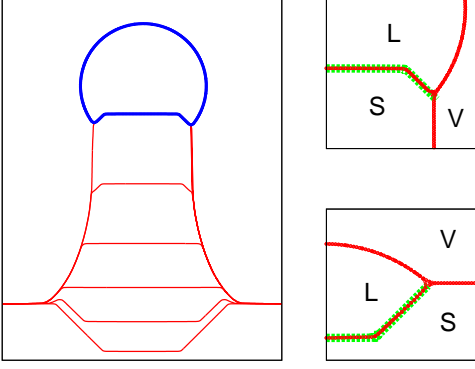


FIG. 13. Phase-field simulation of NW growth from a (10) substrate for $\delta_a = \delta_b = \sqrt{2}/6$, $JW\tau = 0.0028$, and droplet size $A_0/W^2 = 1254$. Outlines of solid are shown at different stages of morphological development in the left panel (as red line). The blue lines depict the liquid-vapor and solid-liquid interfaces at the latest time where the NW is growing in steady-state. The phase-field solid-liquid interface shapes are compared to the prediction of sharp-interface theory (green dashed lines) during steady-state NW growth (top right inset) and for an equilibrium droplet on the substrate (bottom left inset). The three phases are labeled using their corresponding capital letter and all PF interfaces are shown as red lines in the two right panels.

equilibrium shape that is an octagon for a crystal seed surrounded by liquid as shown in the left panel of Fig. 14. To compute the shape in the NW geometry, we apply the anisotropic Young-Herring condition (2) at triple points. Projected onto the x and y axes, this condition yields two independent equations

$$\tilde{\gamma}_{sl}(\theta_f) \cos \theta_f = \cos \psi + \tilde{\gamma}'_{sl}(\theta_f) \sin \theta_f, \quad (116)$$

$$\tilde{\gamma}_{sl}(\theta_f) \sin \theta_f + \tilde{\gamma}'_{sl}(\theta_f) \cos \theta_f + \sin \psi = \tilde{\gamma}_{sv}^0, \quad (117)$$

respectively, where $\tilde{\gamma}_{sv}^0 \equiv \gamma_{sv}^0/\gamma_{lv}^0$. In addition, θ_f and ψ are the angles of the solid-liquid and solid-vapor interfaces measured with respect to the horizontal axis as defined in Fig. 15a. The numerical solution of Eqs. 116 and 117 with $\tilde{\gamma}_{sl} \equiv \gamma_{sl}/\gamma_{lv}^0$ defined by Eq. 112 uniquely determines θ_f and ψ . The solid-liquid interface during NW growth is then the parametric shape defined by Eqs. 116 and 117 for $-\theta_f \leq \theta \leq \theta_f$. This shape is shown in the right panel of Fig. 14. It is also superimposed as a green dashed line in the top-right panel of Fig. 13 and seen to agree well with the steady-state shape with truncated facets predicted by phase-field simulations. Importantly, θ_f and ψ converge to unique values in the sharp cusp $\epsilon \rightarrow 0$ limit. For $\epsilon = 0.01$, those values are almost reached. In particular, $\theta_f \approx 0.783$ is almost $\pi/4$ expected of (11) facets and $\psi \approx 0.832$ is also very close to its $\epsilon \rightarrow 0$ limit derived below. A similar calculation is straightforward to carry out for an equilibrium droplet on a (10) substrate. The predicted shape is also in good quantita-

tive agreement with the phase-field droplet equilibrium shape in the bottom-right panel of Fig. 13 and qualitative agreement with experimental observations showing dissolution of the substrate below the droplet [10].

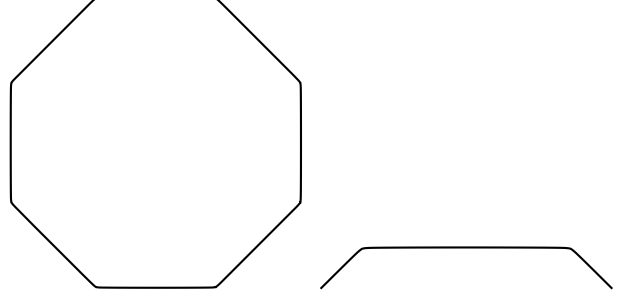


FIG. 14. Computed solid-liquid interface shapes for a crystal seed surrounded by liquid (left) and for the steady-state tip shape of a growing NW in contact with a liquid droplet (right) where the side facets end at triple points. The parameters are $\delta_a = \delta_b = \sqrt{2}/6$, $\epsilon = 0.01$, $\gamma_{sl}^0/\gamma_{lv}^0 = 0.8$, and $\gamma_{sv}^0/\gamma_{lv}^0 = 1.2$.

We now derive analytically the steady-state NW growth shape in the sharp cusp limit ($\epsilon = 0$). In this limit, the truncated (11) and (11) facets have fixed orientations such that $\theta_f = \pi/4$ is no longer an unknown. The unknowns are ψ and the ratio L_B/L_A of the truncated and main facet lengths. To determine those unknowns, we consider small virtual displacements of individual facets of fixed orientations and one of the triple points that leave the total free-energy unchanged, as depicted in Fig. 15. The total free-energy change resulting from a virtual displacement of the main (10) facet a distance h along the direction normal to the facet (Fig. 15b) is the sum of bulk and interface contributions given by

$$\Delta f L_A h + \frac{2\gamma_B h}{\sin \theta_f} - \frac{2\gamma_A h}{\tan \theta_f} = 0, \quad (118)$$

where $\Delta f < 0$ is the difference of free-energy density between solid and liquid, $\gamma_A \equiv \gamma_{sl}(0)$ and $\gamma_B \equiv \gamma_{sl}(\pi/4)$ are the facet free-energies, and the second and third terms corresponds to the change of interface free-energy resulting from the lengthening of the side (11) and (11) facets and the shortening of the main (10) facet, respectively. Similarly, the total free-energy change resulting from the virtual displacement of the (11) facet normal to itself (Fig.15b) is given by

$$\Delta f L_B h + \frac{\gamma_A h}{\sin \theta_f} - \frac{\gamma_B h}{\tan \theta_f} + \frac{(\gamma_{sv}^0 - \gamma_{lv}^0 \sin \psi) h}{\sin(\frac{\pi}{2} - \theta_f)} - \frac{\gamma_B h}{\tan(\frac{\pi}{2} - \theta_f)} = 0, \quad (119)$$

and contains contributions from the changes of length of the (10) and (11) facets as well as the solid-vapor and liquid-vapor interfaces. The virtual displacement of the right triple point (Fig.15c) yields in turn

$$-\gamma_{sv}^0 h \sin \theta_f + \gamma_B h - h \cos(\theta_f + \psi) \gamma_{lv}^0 = 0. \quad (120)$$

Eliminating Δf between Eqs. 118 and (119) yields the prediction of the ratio of facet length

$$\frac{L_B}{L_A} = \frac{\gamma_A \cos \theta_f - \gamma_B + (\gamma_{sv}^0 - \gamma_{lv}^0 \sin \psi) \sin \theta_f}{2 \cos \theta_f (\gamma_B - \gamma_A \cos \theta_f)} \quad (121)$$

with

$$\psi = \cos^{-1} \left(\frac{\gamma_B - \gamma_{sv}^0 \sin \theta_f}{\gamma_{sv}^0} \right) - \theta_f, \quad (122)$$

obtained from Eq. 120. For the parameters of the simulations $\gamma_A = \gamma_B = \gamma_{sl}^0$, $\gamma_{sl}^0/\gamma_{lv}^0 = 0.8$, $\gamma_{sv}^0/\gamma_{lv}^0 = 1.2$, and $\theta_f = \pi/4$, Eq. 122 predicts $\psi \approx 0.826$, which is close to the value $\psi \approx 0.832$ predicted by the rounded-cusp approximation with $\epsilon = 0.01$. In addition, Eq. 121 predicts $L_B/L_A \approx 0.285$ that agrees well quantitatively with both phase-field simulations and sharp interface theory with the rounded cusp approximation.

Finally, the method of virtual displacement can also be used to derive analogous analytical expressions for the ratio of facet lengths and ψ for an equilibrium droplet on a substrate, with ψ defined in Fig. 15d. The calculation is straightforward and we only give here the final results

$$\frac{L_B}{L_A} = \frac{\gamma_A + \gamma_{lv}^0 \cos \psi - \gamma_{sv}^0}{2(\gamma_B - \gamma_A \cos \theta_f)} \quad (123)$$

with

$$\psi = \cos^{-1} \left(\frac{\gamma_{sv}^0 \cos \theta_f - \gamma_B}{\gamma_{lv}^0} \right) - \theta_f, \quad (124)$$

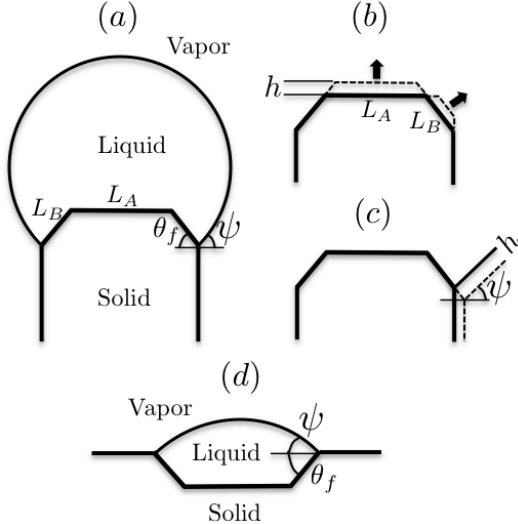


FIG. 15. Schematic representation of (a) steady-state NW growth shape with a main facet of length L_A and two truncated facets of length L_B , (b) virtual displacements of main and right truncated facets, (c) virtual displacement of right triple point, and (d) equilibrium droplet on substrate.

VI. CONCLUSIONS AND OUTLOOK

In summary, we have developed a multi-phase-field model to describe quantitatively NW growth by the vapor-liquid-solid (VLS) process. This model uses a free-energy landscape similar to the one used previously to model eutectic solidification [40] and introduces several new features to adapt this model to the VLS system:

1. The change of catalyst droplet volume, which is associated with the change of concentration of growth atoms inside the droplet, is described using a Lagrange multiplier, in addition to the Lagrange multiplier commonly used to constrain the sum of the phase fields to unity.
2. The physically relevant limit of rapid equilibration of the liquid catalyst to a droplet shape of constant mean curvature on the characteristic time scale of NW growth is achieved by choosing the liquid-vapor interface mobility much larger than the solid-liquid interface mobility. In this limit, the Lagrange multiplier used to constrain the volume of the catalyst reduces to the Laplace pressure inside the droplet, thereby providing a thermodynamically consistent description of the VLS system without the computational burden of treating the catalyst as a real fluid.
3. The driving force for growth is incorporated by adding a non-variational term localized at the solid-liquid interface to the evolution equation for the solid and liquid phase fields, which is equivalent to lowering the free-energy of the solid with respect to the liquid on this binary interface.
4. Anisotropy of the excess interfacial free-energy is introduced by making the free-energy barrier height between two phases dependent on interface orientation.

We have presented a detailed asymptotic analysis of the model in the limit where the interface thickness is much smaller than the NW radius and shown that phase-field equations reduce in this limit to a previously proposed sharp-interface model of NW growth by Schwarz and Tersoff [19]. The simulations reproduce the complex evolution of the interfaces from a droplet on a substrate to steady-state NW growth normal to the substrate with tapering of the side walls. Furthermore, the model can describe different experimentally observed growth regimes including the regime where the growth rate is limited by the solid-liquid interface kinetics, in which case the growth rate depends on the NW radius, and the opposite regime where the growth rate is limited by the incorporation rate of growth atoms at the catalyst surface, in which case the growth rate is independent of radius.

With the incorporation of an anisotropic solid-liquid γ -plot that contains faceted interfaces, the model can also reproduce the characteristic solid-liquid interface NW tip

shape consisting of a main facet intersected by two truncated side facets ending at triple points, as well as more complex growth behaviors including NW kinking and crawling. Finally, we have developed a sharp-interface theory to predict the length of the main facet and truncated facet and shown that the predictions are in good agreement with phase-field simulations.

While the simulations presented in this paper were restricted to two dimensions, the present PF model can be readily implemented in three dimensions to carry out a quantitative comparison with experimentally observed NW growth shapes. Three-dimensional simulation results in the Si-Au VLS system will be presented elsewhere. Another interesting prospect is to extend the proposed theoretical description of faceted NW growth shape to three dimensions.

VII. ACKNOWLEDGEMENT

This research was supported by the National Science Foundation grant 1106214 from the DMR CMMT Program.

Appendix A: Derivation of the Lagrange multiplier controlling the catalyst volume

In this PF NW growth model, the catalyst size constraint is incorporated by adding a Lagrange multiplier λ_A to the original free energy functional F

$$\tilde{F} = F - \lambda_A h \left[\int g_l(\vec{\phi}) dv - A(t) \right], \quad (\text{A1})$$

where A is the droplet volume at time t and g_l is a function given in the main text that varies smoothly between 1 in the liquid and 0 in other phases such that $\int g_l(\vec{\phi}) dv$ measures the total droplet volume. Minimization of \tilde{F} with respect to ϕ gives a configuration where the total catalyst volume (measured by the integral of g_l) is constrained to be $A(t)$. The evolution equation derived from \tilde{F} is

$$\tau \frac{\partial \phi_i}{\partial t} = -\bar{K}(\vec{\phi}) h^{-1} \left(\frac{\delta \tilde{F}}{\delta \phi_i} - \lambda_A h \frac{\partial g_l}{\partial \phi_i} \right), \quad (\text{A2})$$

where the modified functional derivative $\frac{\delta \tilde{F}}{\delta \phi_i}$ are defined by Eqs. 16 to 18. The other constraint $\sum_{i=1}^3 \phi_i = 1$ can be included by adding a summation term to the equation of motion [40]

$$\tau \frac{\partial \phi_i}{\partial t} = -K(\vec{\phi}) h^{-1} \left(\frac{\delta \tilde{F}}{\delta \phi_i} - \frac{1}{3} \sum_{j=1}^3 \frac{\delta \tilde{F}}{\delta \phi_j} \right). \quad (\text{A3})$$

A given droplet volume evolution

$$\frac{dA}{dt} = \frac{d}{dt} \int g_l(\vec{\phi}) dv = \dot{A}, \quad (\text{A4})$$

can be written as

$$\int \frac{\partial g_l(\vec{\phi})}{\partial t} dv = \int \sum_{i=1}^2 \left(\frac{\partial \tilde{g}_l}{\partial \phi_i} \frac{\partial \phi_i}{\partial t} \right) dv, \quad (\text{A5})$$

by moving the time derivative inside the integral. Since the phase fraction condition $\sum_{i=1}^3 \phi_i = 1$ is enforced in the dynamics, g_l is replaced by \tilde{g}_l that depends only on two phase fields. Using $\partial \phi_i / \partial t$ in Eq. A3, one can rewrite Eq. A5 as

$$\begin{aligned} \dot{A} \tau = & - \int K h^{-1} \left\{ \sum_{i=1}^2 \frac{\delta \tilde{F}}{\delta \phi_i} \frac{\partial \tilde{g}_l}{\partial \phi_i} - \frac{1}{3} \sum_{i=1}^2 \frac{\partial \tilde{g}_l}{\partial \phi_i} \sum_{j=1}^3 \frac{\delta \tilde{F}}{\delta \phi_j} \right. \\ & \left. - \lambda_A h \left[\sum_{i=1}^2 \left(\frac{\partial \tilde{g}_l}{\partial \phi_i} \right)^2 - \frac{1}{3} \left(\sum_{i=1}^2 \frac{\partial \tilde{g}_l}{\partial \phi_i} \right)^2 \right] \right\} dv, \end{aligned} \quad (\text{A6})$$

where g_l in \tilde{F} is also replaced by \tilde{g}_l . Solving for λ_A using Eq. A6 gives

$$\lambda_A = \frac{I_1 - I_2 + \dot{A} \tau}{I_3 - I_4}, \quad (\text{A7})$$

with

$$I_1 = \int K h^{-1} \sum_{i=1}^2 \frac{\delta \tilde{F}}{\delta \phi_i} \frac{\partial \tilde{g}_l}{\partial \phi_i} dv, \quad (\text{A8})$$

$$I_2 = \frac{1}{3} \int K h^{-1} \sum_{i=1}^2 \frac{\partial \tilde{g}_l}{\partial \phi_i} \sum_{j=1}^3 \frac{\delta \tilde{F}}{\delta \phi_j} dv, \quad (\text{A9})$$

$$I_3 = \int K \sum_{i=1}^2 \left(\frac{\partial \tilde{g}_l}{\partial \phi_i} \right)^2 dv, \quad (\text{A10})$$

$$I_4 = \frac{1}{3} \int K \left(\sum_{i=1}^2 \frac{\partial \tilde{g}_l}{\partial \phi_i} \right)^2 dv. \quad (\text{A11})$$

Appendix B: Sharp-interface limit for an isolated droplet with volume constraint

The sharp-interface limit of a single order-parameter PF model with a volume-controlling Lagrange multiplier is worked out in this section. This case corresponds physically to an isolated liquid droplet inside the vapor phase. The main purpose of this appendix is to understand the role of this Lagrange multiplier λ_A in this simpler setting. The same formulation is used to control the catalyst size in our multiphase-field VLS NW growth model. The sharp-interface limit of this model is examined in section IV using results derived in this appendix.

The free-energy is given by

$$F_1 = \int h \left[\frac{W^2}{2} |\nabla \phi|^2 + f(\phi) \right] dv, \quad (\text{B1})$$

with $f(\phi)$ being a double-well potential which has two minima at $\phi = 0$ and $\phi = 1$ corresponding to the vapor and liquid phase, respectively. The evolution equation for the phase field ϕ is

$$\tau \frac{\partial \phi}{\partial t} = -K_1(\phi) h^{-1} \left(\frac{\delta F_1}{\delta \phi} - \lambda_A \frac{\partial g}{\partial \phi} \right), \quad (\text{B2})$$

where g is a smooth tilt function (similar to g_l in the multiphase-field model) that varies smoothly between 0 and 1, $K_1(\phi)$ is the dimensionless mobility (similar to $K(\vec{\phi})$ in the multiphase-field model), and

$$\lambda_A = \frac{\int K_1(\phi) h^{-1} \frac{\delta F_1}{\delta \phi} \frac{\partial g}{\partial \phi} dv + \dot{A} \tau}{\int K_1 \left(\frac{\partial g}{\partial \phi} \right)^2 dv}, \quad (\text{B3})$$

is a volume-controlling Lagrange multiplier, which is derived using the approach outlined in appendix A. Using Eq. B1, Eq. B2 becomes

$$\tau \frac{\partial \phi}{\partial t} = K_1 \left[W^2 \nabla^2 \phi - \frac{\partial f}{\partial \phi} + \lambda_A \frac{\partial g}{\partial \phi} \right]. \quad (\text{B4})$$

To get the corresponding sharp-interface limit of Eq. B4, a sharp-interface analysis is carried out in the following. Unlike the method used in the sharp-interface expansion of PF solidification models where both outer and inner expansions are performed [38, 48], only an inner expansion on the scale of the interface thickness is needed here since the interface dynamics is not controlled by a long range diffusion field.

In order to characterize the motion of the interface, we define the local curvilinear coordinate system (r, s) where $r(x, y, t)$ and $s(x, y, t)$ measure the position along a direction \hat{r} normal to the interface (where \hat{r} points to the $\phi = 0$ phase) and along a direction \hat{t} parallel to constant ϕ contours (along the interface) in a frame moving at the normal velocity of the interface. In this coordinate system, the $\nabla^2 \phi$ term in Eq. B4 reduces to

$$\nabla^2 \phi = \frac{\partial^2 \phi}{\partial r^2} + \kappa \frac{\partial \phi}{\partial r} + (\nabla s)^2 \frac{\partial^2 \phi}{\partial s^2} + \nabla^2 s \frac{\partial \phi}{\partial s}, \quad (\text{B5})$$

where $\nabla^2 r = \kappa$ and $|\nabla r| = 1$ are used in derivation. Since (r, s) are defined in a moving frame, the time derivative $\partial \phi / \partial t$ in Eq. B4 is replaced by

$$\frac{\partial \phi}{\partial t} \rightarrow \frac{\partial \phi}{\partial t} + \frac{\partial r}{\partial t} \frac{\partial \phi}{\partial r} + \frac{\partial s}{\partial t} \frac{\partial \phi}{\partial s}. \quad (\text{B6})$$

To study the motion of ϕ in the sharp-interface limit, a mesoscopic length l_c is introduced such that the interface thickness W is small comparing with l_c or $p = W/l_c \rightarrow 0$. Rescaling Eq. B4 with length scale l_c and time scale l_c^2/D (where D has the dimension of interface mobility M times the surface energy γ), we obtain

$$\alpha p^2 \frac{\partial \phi}{\partial t} = p^2 \nabla^2 \phi - \frac{\partial f}{\partial \phi} + \lambda_A \frac{\partial g}{\partial \phi}, \quad (\text{B7})$$

where $\alpha = \tau D / (W^2 K_1)$. Using Eqs. B5 and B6, Eq. B7 becomes

$$\begin{aligned} \alpha p^2 \left(\frac{\partial \phi}{\partial t} - \frac{\partial \phi}{\partial r} v + \frac{\partial \phi}{\partial s} \frac{\partial s}{\partial t} \right) &= p^2 \left[\frac{\partial^2 \phi}{\partial r^2} + \kappa^0 \frac{\partial \phi}{\partial r} \right. \\ &\quad \left. + (\nabla s)^2 \frac{\partial^2 \phi}{\partial s^2} + \nabla^2 s \frac{\partial \phi}{\partial s} \right] \\ &\quad - \frac{\partial f}{\partial \phi} + \lambda_A \frac{\partial g}{\partial \phi}, \end{aligned} \quad (\text{B8})$$

where $v = -\partial r / \partial t$ and $\kappa^0 = \kappa l_c$ is the scaled curvature. Next, a stretched variable $z = r/p$ is introduced such that it maps the interface region into $(-\infty, +\infty)$ in z . Using this new variable z , Eq. B8 becomes

$$\begin{aligned} \alpha p^2 \left(\frac{\partial \phi}{\partial t} - \frac{1}{p} \frac{\partial \phi}{\partial z} v + \frac{\partial \phi}{\partial s} \frac{\partial s}{\partial t} \right) &= p^2 \left[\frac{1}{p^2} \frac{\partial^2 \phi}{\partial z^2} + \kappa^0 \frac{1}{p} \frac{\partial \phi}{\partial z} \right. \\ &\quad \left. + (\nabla s)^2 \frac{\partial^2 \phi}{\partial s^2} + \nabla^2 s \frac{\partial \phi}{\partial s} \right] \\ &\quad - \frac{\partial f}{\partial \phi} + \lambda_A \frac{\partial g}{\partial \phi}. \end{aligned} \quad (\text{B9})$$

Keeping only $O(p)$ terms, Eq. B9 is reduced to

$$-\alpha p \phi_z v = \phi_{zz} + p \kappa^0 \phi_z - q(\phi) + \lambda_A \frac{\partial g}{\partial \phi}, \quad (\text{B10})$$

where ϕ_z and ϕ_{zz} are the first and the second derivative of ϕ with respect to z , and $q(\phi) = \partial f / \partial \phi$. All s related terms are dropped since they are all of $O(p^2)$. The phase field ϕ can also be expanded in the small parameter p

$$\phi = \phi^0 + p \phi^1 + p^2 \phi^2 + \dots \quad (\text{B11})$$

With this expansion, Eq. B10 is further reduced to

$$\begin{aligned} -\alpha p \phi_z^0 v &= \phi_{zz}^0 + p \phi_{zz}^1 + p \kappa^0 \phi_z^0 - q(\phi^0) - q'(\phi^0) p \phi^1 \\ &\quad + \lambda_A g'(\phi^0), \end{aligned} \quad (\text{B12})$$

where q' and g' denote the derivatives of q and g with respect to ϕ , respectively. Since the interface velocity v only appears in the $O(p)$ term on the left-hand-side of Eq. B12, stationary interface properties of the model are given by $O(1)$ terms in Eq. B12. Since, furthermore, the Lagrange multiplier λ_A is used to control liquid volume in dynamics, it should only appear at the same (or higher) order of the interface velocity, i.e. $\lambda_A = p \lambda_A^1 + O(p^2)$. To $O(1)$, Eq. B12 becomes

$$\phi_{zz}^0 - q(\phi^0) = 0. \quad (\text{B13})$$

where $f = \phi^2(1 - \phi)^2$ gives $q(\phi) = 2\phi(1 - \phi)(1 - 2\phi)$. Solution of Eq. B13 gives the stationary phase boundary profile

$$\phi^0(z) = \frac{1}{2} \left[1 - \tanh \left(\frac{z}{\sqrt{2}} \right) \right]. \quad (\text{B14})$$

To $O(p)$, Eq. B12 is

$$-(\alpha v + \kappa^0) \phi_z^0 - \lambda_A^1 g'(\phi^0) = \phi_{zz}^1 - q'(\phi^0) \phi^1. \quad (\text{B15})$$

Defining a linear operator

$$L \equiv \frac{\partial^2}{\partial z^2} - q'(\phi^0), \quad (\text{B16})$$

Eq. B15 can be rewritten as

$$L\phi^1 = -(\alpha v + \kappa^0)\phi_z^0 - \lambda_A^1 g'(\phi^0). \quad (\text{B17})$$

Eq. B13 implies that ϕ_z^0 is a zero mode of the linear operator L (eigenfunction with zero eigenvalue) since

$$L\phi_z^0 = \phi_{zzz}^0 - q'(\phi^0)\phi_z^0 = 0. \quad (\text{B18})$$

Furthermore, since L is self-adjoint, the right-hand-side of Eq. B17 must be orthogonal to the null space of L for a nontrivial solution of Eq. B17 to exist, which yields the standard solvability condition

$$\int_{-\infty}^{+\infty} \phi_z^0 [-(\alpha v + \kappa^0)\phi_z^0 - \lambda_A^1 g'(\phi^0)] dz = 0, \quad (\text{B19})$$

which can be further simplified to

$$v = \frac{-\kappa^0 \gamma^0 + \lambda_A^1}{Q}, \quad (\text{B20})$$

with $\gamma^0 = \int_{-\infty}^{+\infty} (\phi_z^0)^2 dz$ and $Q = \int_{-\infty}^{+\infty} \alpha (\phi_z^0)^2 dz$. By replacing v and κ^0 with their unscaled dimensional form $v = Vl_c/D$, $\kappa^0 = l_c \kappa$, and using the dimensional surface energy $\gamma = Wh\gamma^0$, Eq. B20 becomes

$$V = M(-\kappa\gamma + \lambda_A h), \quad (\text{B21})$$

with mobility

$$M = \frac{W}{\tau h} \frac{1}{\int_{-\infty}^{+\infty} (\phi_z^0)^2 K_1^{-1} dz}. \quad (\text{B22})$$

Up to now, the sharp interface expression of λ_A is still unknown. Using the volume control condition (Eq. A4) with $g_l(\vec{\phi})$ replaced by $g(\phi)$ and the coordinate transform in Eq. B6, we have

$$\int g' \left(\frac{\partial \phi}{\partial t} - V \frac{\partial \phi}{\partial r} + \frac{\partial \phi}{\partial s} \frac{\partial s}{\partial t} \right) ds dr = \dot{A}, \quad (\text{B23})$$

where the volume integral has been replaced by

$$dv \rightarrow ds dr, \quad (\text{B24})$$

with elements of arclength and radial coordinates ds and dr , respectively. It is important to note that the dimensional velocity V is used here since time and space are not rescaled. With the stretched coordinate transform $z = r/p$, keeping only the leading order terms on the left-hand-side gives

$$- \int g' \phi_z V ds dz = \dot{A}. \quad (\text{B25})$$

Replacing V with Eq. B21, the Lagrange multiplier is then

$$\lambda_A h = \frac{\dot{A}}{MS} + \frac{\gamma \int \kappa ds}{S}, \quad (\text{B26})$$

where $S = \int ds$ is the length of the interface. Using Eq. B26, Eq. B21 becomes

$$V = M \left(-\kappa\gamma + \gamma \frac{\int \kappa ds}{S} \right) + \frac{\dot{A}}{S}, \quad (\text{B27})$$

which is the droplet evolution Eq. 55.

Appendix C: Incorporation of anisotropic solid-liquid interfacial free-energy and facets

We consider a solid-liquid γ -plot of the form energy function

$$\gamma_{sl}(\theta) = \gamma^0 [1 + \delta_a |\sin 2\theta| + \delta_b |\cos 2\theta|], \quad (\text{C1})$$

where θ is the angle of the interface normal direction with respect to a reference crystal axis. According to the Wulff construction, this γ -plot yields an equilibrium crystal shape with two sets of (10) and (11) facets at that are shown in the left of Fig. 14.

To incorporate the interface free-energy anisotropy in Eq. C1 into the multiphase-field model, we treat a_i in Eq. 29 as an orientation-dependent parameter $a_i(\theta)$ where θ is the interface orientation angle. Since there are two PF variables (ϕ_j and ϕ_k) involved at a binary interface in this model, the interface orientation can be expressed using either

$$\sin \theta_j = -\partial_y \phi_j / |\nabla \phi_j|, \quad (\text{C2})$$

or

$$\sin \theta_k = -\partial_y \phi_k / |\nabla \phi_k|. \quad (\text{C3})$$

Since the barrier term f_a^i is symmetric under the exchange of ϕ_j and ϕ_k , the same property should hold for $a_i(\theta)$. A simple choice is then

$$a_i(\theta) = \left[\frac{1}{2} a_i(\theta_j) + \frac{1}{2} a_i(\theta_k) \right], \quad (\text{C4})$$

which averages the contribution from both ϕ_j and ϕ_k . From here, the functional derivative is given by

$$\frac{1}{h} \frac{\delta F}{\delta \phi_i} = \frac{\partial f_d^i}{\partial \phi_i} - W^2 \nabla^2 \phi_i + \sum_{l=1}^3 \left[a_l \frac{\partial f_a^l}{\partial \phi_i} + b_l \frac{\partial f_b}{\partial \phi_i} \right. \\ \left. + \frac{\partial}{\partial x} \left(\frac{\phi_{i,y}}{|\nabla \phi_i|^2} f_a^l a_{l,i} \right) - \frac{\partial}{\partial y} \left(\frac{\phi_{i,x}}{|\nabla \phi_i|^2} f_a^l a_{l,i} \right) \right], \quad (\text{C5})$$

where we have defined

$$a_{l,i} = \frac{1}{2} \frac{\partial a_l(\theta_i)}{\partial \theta_i}, \quad \phi_{i,x} = \frac{\partial \phi_i}{\partial x}. \quad (\text{C6})$$

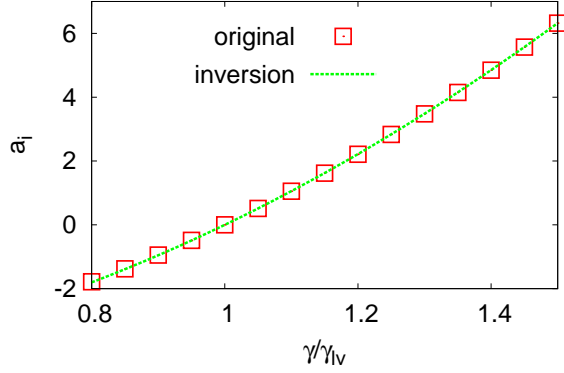


FIG. 16. Comparison of free-energy barrier height parameter a_i versus dimensionless interface energy γ/γ_{lv} computed using the inversion formula Eq. C9 (green line), which predicts a_i as a function of γ/γ_{lv} , and Eq. C8 (red square), which predicts γ/γ_{lv} as a function of a_i . The inversion formula can be used to choose a_i in the PF model to reproduce an arbitrary form of interface energy anisotropy.

In the numerical implementation, the orientation dependent terms are only calculated in the interface region that is defined by $|\nabla\phi_i| < \epsilon_i$ where ϵ_i is a small cutoff.

In general, $a_i(\theta)$ needs to be computed to quantitatively reproduce a prescribed form of interface free-energy anisotropy. For this, we start from the relation between $a_i(\theta)$ and $\gamma_{jk}(\theta)$ given by

$$\frac{\gamma_{jk}(\theta)}{Wh} \equiv \tilde{\gamma}_{jk} = 2\sqrt{2} \int_0^1 p(1-p) \sqrt{1 + a_i(\theta)p(1-p)} dp, \quad (\text{C7})$$

which can be reduced to

$$\tilde{\gamma}_{jk} = 2\sqrt{2} \times \frac{2\sqrt{a_i}(4 + 3a_i) + (4 + a_i)(3a_i - 4) \cot^{-1}(2/\sqrt{a_i})}{64a_i^{3/2}}, \quad (\text{C8})$$

by carrying out the integral. Eq. C8 is a transcendental equation and cannot be inverted analytically to find a_i as a function of $\tilde{\gamma}_{jk}$. However, a plot of a_i versus $\tilde{\gamma}_{jk}$ using Eq. C8 shows that the inverse function $a_i(\tilde{\gamma}_{jk})$ is very accurately fitted over a wide range of a_i up to 100 by a simple quadratic polynomial.

$$a_i = B_0 + B_1\tilde{\gamma}_{jk} + B_2\tilde{\gamma}_{jk}^2, \quad (\text{C9})$$

with $B_0 = -4.86349$, $B_1 = -0.693313$ and $B_2 = 23.3564$. For the γ range we used in this work, accuracy of the quadratic inversion formula is shown in Fig. 16

The anisotropic surface energy in Eq. C1 also needs to be regularized since $d\gamma/d\theta$ becomes infinite at a sharp cusp. A simple regularized form is

$$\gamma(\theta) = \gamma^0 [1 + \delta_a \sqrt{\sin^2 2\theta + \epsilon^2} + \delta_b \sqrt{\cos^2 2\theta + \epsilon^2}], \quad (\text{C10})$$

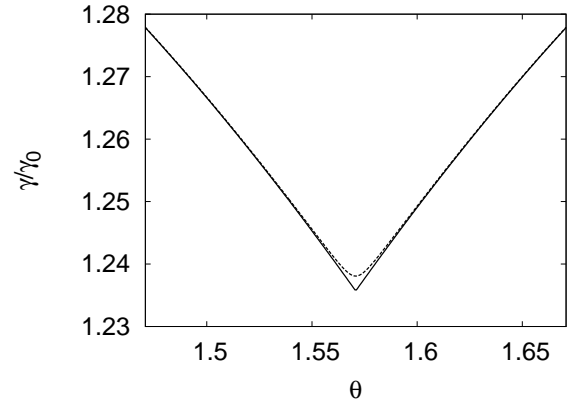


FIG. 17. Regularization of the γ -plot near a cusp with $\delta_a = \delta_b = \sqrt{2}/6$ and $\epsilon = 0.01$. The solid line is the original γ plot given by Eq. C1. The dashed line is the regularized γ plot given by Eq. C10.

which is compared to the form of γ with sharp cusps in Fig. 17. The regularization parameter $\epsilon = 0.01$ and interface cutoff $W\epsilon_i = 10^{-5}$ are used in all the numerical simulations with the anisotropic model.

-
- [1] V. Schmidt, J. V. Wittemann, and U. Gösele, *Chem. Rev.* **110**, 361-388 (2010).
 [2] R. Ruruli, *Rev. Mod. Phys.* **82**, 427 (2010).
 [3] S. A. Fortuna and X. Li, *Semicond. Sci. Technol.* **25**, 024005 (2010).
 [4] J. B. Hannon, S. Kodambaka, F. M. Ross and R. M. Tromp, *Nature* **440**, 69 (2006).
 [5] S. Kodambaka, J. Tersoff, M. C. Reuter and F. M. Ross, *Phys. Rev. Lett.* **96**, 096105 (2006).
 [6] Y. Chou, W. Wu, S. Cheng, B. Yoo, N. Myung, L. J. Chen and K. N. Tu, *Nano Lett.* **8**, 2194 (2008).
 [7] V. Schmidt, S. Senz and U. Gösele, *Nano Lett.* **5**, 931 (2005).
 [8] H. Adhikari, A. F. Marshall, C. E. Chidsey and P. C. McIntyre, *Nano Lett.* **6**, 318 (2006).
 [9] P. Madras, E. Dailey and J. Drucker, *Nano Lett.* **9**, 3826 (2009).
 [10] N. Ferralis, R. Maboundian and C. Carraro, *J. Am. Chem. Soc.* **130**, 2681 (2008).
 [11] F. M. Ross, J. Tersoff and M. C. Reuter, *Phys. Rev. Lett.* **95**, 146104 (2005).
 [12] E. I. Givargizov, *J. Crst. Growth* **31**, 20 (1975).
 [13] V. Schmidt, S. Senz, and U. Gösele, *Phys. Rev. B* **75**, 045335 (2007).
 [14] L. E. Fröberg, W. Seifert and J. Johansson, *Phys. Rev. B* **76**, 153401 (2007).

- [15] V. G. Dubrovskii, N. V. Sibirev, J. C. Harmand, and F. Glas, *Phys. Rev. B* **78**, 235301 (2008)
- [16] S. M. Roper, S. H. Davis, S. A. Norris, A. A. Golovin, P. W. Voorhees and M. Weiss, *J. Appl. Phys.* **102**, 034304 (2007).
- [17] S. M. Roper, A. M. Anderson, S. H. Davis and P. W. Voorhees, *J. Appl. Phys.* **107**, 114320 (2010).
- [18] S. Muralidharan, P. W. Voorhees, and S. H. Davis, *J. App. Phys.* **114**, 114305 (2013).
- [19] K. W. Schwarz and J. Tersoff, *Phys. Rev. Lett.* **102**, 206101 (2009).
- [20] K. W. Schwarz and J. Tersoff, *Nano Lett.* **11**, 316 (2011).
- [21] K.W. Schwarz, J. Tersoff, S. Kodambaka, Y.-C. Chou, and F. M. Ross, *Phys. Rev. Lett.* **107**, 265502 (2011).
- [22] K. W. Schwarz and J. Tersoff, *Nano Lett.* **12**, 1329 (2012).
- [23] K.W. Schwarz, J. Tersoff, S. Kodambaka, and F. M. Ross, *Phys. Rev. Lett.* **113**, 055501 (2014).
- [24] N. Wang, PhD Thesis (Northeastern University, Boston, 2011).
- [25] E. J. Schwalbach, S. H. Davis, P. W. Voorhees, D. Wheeler, and J. A. Warren, *J. Mater. Res.* **26**, 2186 (2011)
- [26] E. J. Schwalbach, S. H. Davis, P. W. Voorhees, J. A. Warren, and D. Wheeler, *J. Appl. Phys.* **111**, 024302 (2012)
- [27] Y. Wang, S. Ryu, P. C McIntyre, and W. Cai, *Modelling Simul. Mater. Sci. Eng.* **22**, 055005 (2014)
- [28] T. Haxhimali, D. Buta, M. Asta, P. W. Voorhees and J. J. Hoyt, *Phys. Rev. E* **80**, 050601(R) (2009).
- [29] H. Wang, L. A. Zepeda-Ruiz, G. H. Gilmer and M. Upmanyu, *Nature Comm.* **4**, 1956 (2013).
- [30] T. Frolov, W. C. Carter, and M. Asta, *Nano Lett.* **14**, 3577 (2014).
- [31] W. J. Boettinger, J. A. Warren, C. Beckermann and A. Karma, *Annu. Rev. Mater. Res.* **32**, 163 (2002).
- [32] L. Q. Chen, *Annu. Rev. Mater. Res.* **32**, 113 (2002).
- [33] I. Steinbach, *Modelling Simul. Mater. Sci. Eng.* **17**, 073001 (2009)
- [34] Y. Mishin, W. J. Boettinger, J. A. Warren and G. B. McFadden, *Acta Mater.* **57**, 3771 (2009).
- [35] Y. Kim, N. Provatas, N. Goldenfeld, J. Dantzig. *Phys. Rev. E* **59**, R2546-R2549 (1999).
- [36] Y. Wang and J. Li, *Acta Mater.* **58**, 1212-1235 (2010).
- [37] A. Karma, D. Kessler and H. Levine, *Phys. Rev. Lett.* **87**, 045501 (2001).
- [38] A. Karma, *Phys. Rev. Lett.* **87**, 115701 (2001).
- [39] T. Haxhimali, A. Karma, F. Gonzales and M. Rappaz, *Nature Materials* **5**, 660 (2006).
- [40] R. Folch and M. Plapp, *Phys. Rev. E* **72**, 011602 (2005).
- [41] J. Debierre, A. Karma, F. Celestini, and R. Guerin, *Phys. Rev. E* **68**, 041604 (2003).
- [42] C. Herring, *The Physics of Powder Metallurgy*, ed. by W. E. Kingston (McGraw-Hill, New York, 1951), p. 143.
- [43] A. A. Wheeler and G. B. McFadden, *Eur. J. Appl. Math.* **7**, 367 (1996).
- [44] J. J. Eggleston, G. B. McFadden and P. W. Voorhees, *Physica D* **150**, 91 (2001).
- [45] S. Torabi, J. Lowengrub, A. Voigt and S. Wise, *Proc. R. Soc. A* **465**, 1337 (2009).
- [46] R. Kobayashi, *Physica D* **63**,410 (1993).
- [47] G. B. McFadden, A. A. Wheeler, R. J. Braun, S. R. Coriell and R. F. Sekerka, *Phys. Rev. E* **48**, 2016 (1993).
- [48] A. Karma and Wouter-Jan Rappel, *Phys. Rev. E* **57**, 4323 (1998).
- [49] D. J. Eaglesham, A. E. White, L. C. Feldman, N. Moriya and D. C. Jacobson, *Phys. Rev. Lett.* **70**, 1643 (1993).
- [50] P. W. Voorhees, S. R. Coriell, G. B. McFadden and R. F. Sekerka, *J. Cryst. Growth* **67**, 425 (1984).